ABSTRACT

SCHALL, JAMES DAVID. Computational Modeling: Nanoindentation and An *Ad Hoc* Molecular Dynamics-Finite Difference Thermostat (Under the direction of Donald W. Brenner.)

Due to anharmonicities in atomic interactions it is expected that the indentation modulus should very with pre-existing stress in the substrate. However, Tsui, Pharr and Oliver have shown in experiment that the indentation modulus for indentations where plasticity is present is essentially independent of the pre-existing stress if the true contact area is used to make the calculation. They show that the dependence is due to errors in the empirical estimates used to determine contact area. Their experiment is repeated using molecular dynamics simulation and the results of various empirical estimates for the contact area have been compared to the true contact determined from the simulation. The results show that the empirical estimates lead to large errors in contact area. As a result, the hardness and modulus are in error. When true contact areas are used the results agree with experiment. By using shallow elastic indentations, it is shown that indentation can be used to predict the true dependence of pre-stress on the indentation modulus predicted given the knowledge of the anharmonicity in the atomic potential which may be predicted using molecular statics calculations. In addition, a new method for temperature control in molecular dynamics simulations is presented. In metals, electronic interactions account for the majority of the heat flow. Approaches such as the embedded atom method do not account for electrons explicitly and thermal transport cannot be accurately modeled. To overcome this, an *ad hoc* feedback between the molecular dynamics simulation and the continuum heat flow equation has been developed. The method relies on experimental values for the thermal conductivity

and heat capacity as inputs for a finite difference solution to the continuum equation. The thermostat was tested for a simple quasi one-dimensional case. Results are in excellent agreement with the analytical solution for heat flow. The method was extended to three dimensions and applied to the problem of substrate heating due to tip sliding. Although the temperature changes in the substrate due to the sliding tip are small, results show significant differences in the force felt by the tip when the thermostat is turned on or off.

COMPUTATIONAL MODELING: NANOINDENTATION AND AN *AD HOC* MOLECULAR DYNAMICS-FINITE DIFFERENCE THERMOSTAT

by
JAMES DAVID SCHALL

A dissertation submitted to the Graduate Faculty o
North Carolina State University
in partial fulfillment of the
requirements for the Degree of
Doctorate of Philosophy

MATERIALS SCIENCE AND ENGINEERING

Raleigh

2004

APPROVED BY:

_____ _____

_____ _____

Chair of Advisory Committee

DEDICATION

To my wife Christine: A gift of paper for our first anniversary May 24, 2004.

BIOGRAPHY

James David Schall, born November 16, 1972 in Knoxville TN, spent most of his younger years smashing remote control cars, radios, etc. with hammers to see how the insides worked. By age ten he had pretty much derived $F=ma$ from first principles (not knowing at the time that some guy named Newton had already done so a few hundred years prior). As he grew older, he started using tools with somewhat more finesse, screwdrivers, soldering irons, etc., and eventually started putting the things he disassembled back together again (and sometimes they would even work). In 1990, National Geographic Magazine published an issue devoted to Materials Science and Engineering and a career was born. In 1991, Schall graduated from Karns High School in Knoxville, Tennessee and went on to attend the University of Tennessee, Knoxville. He later transferred to North Carolina State University where he earned his Bachelors of Science in Materials Science and Engineering in 1997, graduating magna cum laud. He continued at North Carolina State receiving his Masters of Science in May, 2000 and PhD. in 2004.

ACKNOWLEDGEMENTS

I would like to thank all those who have assisted me in this work, particularly my advisor Don Brenner, and my committee members, Ron Scattergood, Phil Russell, and Chris Roland. I would also like to thank Bobby Sumpter, Don Noid, and George Pharr for hosting me at ORNL, and Steve Plimpton at SNL for the use of his code PARADYN. I would like to acknowledge SURA and NSF for financial support. In addition, I would like to acknowledge my coworkers, O. Shenderova, J. Mewkill, C. Padgett, S. Adiga, and G. Hogshead for there additional brain power. Last but not least I'd like to thank my family and friends for their support.

TABLE OF CONTENTS

LIST OF TABLES

LIST OF FIGURES

LIST OF SYMBOLS AND ABBREVIATIONS

EAM: Embedded Atom Method

FD: Finite Difference

FS: Field and Swain method

GLE: Generalized Langevin Equation

IP: Inscribed polygon method

MD: Molecular Dynamics

OP: Oliver-Pharr method

TPO: Tsui, Pharr and Oliver

1. INTRODUCTION

1.1 General introduction

In his famous talk "There's plenty of room at the bottom" Richard Feynman[1] predicted that in the near future we would be designing useful structures and devices from the bottom up, starting at the most basic of levels – the atomic scale - using molecular building blocks. Rapid progress in areas such as self-assembly, molecular electronics, and DNA research have made his dream a reality. Driven in part by the semiconductor industry, the top-down approach has made rapid advances as well. Take for instance a recent INTEL chip design[2], illustrated in FIG. 1.1a. Dimensions of the gate region are on the order of 50 x 25 nm, while the oxide layer itself is approximately 1.2 nm thick. The design relies on strain imposed by the lattice mismatch between the oxide layer and the silicon in the gate region to control the channel width for the transistor, clearly an atomic scale phenomenon. Another example, springboarding from the patterning and etching techniques developed of the semiconductor industry, are micro-electrical-mechanical systems (MEMS)[3]. These micron-scaled machines typically mimic traditional full-scale mechanical devices with systems of gears and pinions, sliders and ratchets. The operational lifetime of such devices is dominated by interactions at the atomic level, particularly sliding interfaces with atomic and nanoscale surface features as suggested by the diagram shown in FIG 1.1b.

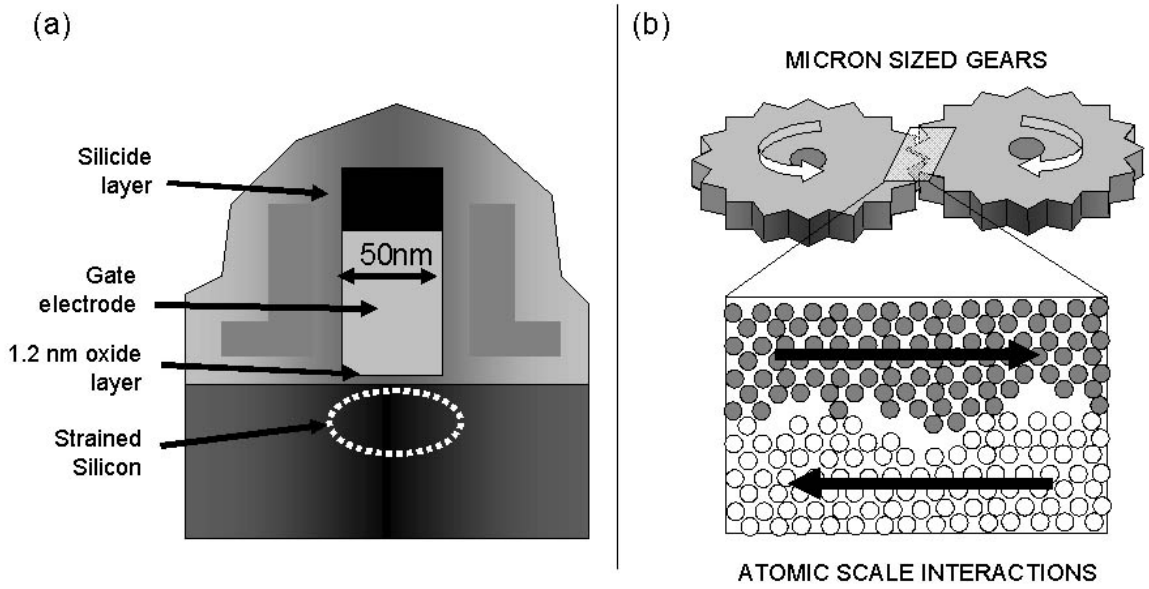

FIGURE 1.1: Examples of nanoscale features. a) Schematic diagram of a 90 nm transistor showing the location of the strained silicon channel [2]. b) Schematic illustration of a simple MEMS gear illustrating atomic scale contact regimes at the points of gear contact.

The semiconductor industry is not the only driving force towards this atomic scale miniaturization. Recent advances in metallurgical processing have allowed grain refinements down to grain sizes of 10-100 nm[4]. The mechanical behavior of these nanocrystalline materials remains controversial. Observations ranging from greatly enhanced ductility to dramatically increased yield strength due to the Hall-Petch effect have been reported. However, most agree that below a critical grain size of approximately 30 nm, a phenomenon known as the inverse Hall-Petch effect is occurs. In these materials, the conventional dislocation slip mechanism ceases in favor of a grain-boundary based deformation mechanism. Below this critical grain size, the yield and flow stresses actually decrease with decreasing grain size. A debate remains as to whether the deformation mechanism involves grain boundary sliding or grain boundary creep.

Thin film materials also exhibit unique behaviors often quite different from their parent materials. Below a certain thickness, the substrate may play a role in the thin film's properties. One commonly used tool for investigating thin film properties is load-sensing indentation or nanoidentation. Often residual strains exist in the film due to processing and lattice mismatch. This strain can strongly influence the data obtained from nanoindentation tests making characterization and comparison of films challenging [5].

This general bottom-up and top-down convergence towards nanoscale devices and materials creates a new set of engineering challenges. In general, as the atomic scale is approached traditional continuum concepts breakdown, and surface and interfacial effects tend to dominate materials properties, although in ways that are not always clearly understood. New methods are required for analyzing, characterizing, and understanding microstructure and mechanical properties. All the while computational power has been increasing making it possible to model systems with dimensions on the order of 10-100 nm, feature sizes now relevant to engineers. The recent nexus between this decrease in feature size and increase in computational power now makes computer simulation a powerful tool for addressing these challenges.

In this thesis, molecular dynamics simulation has been used to study the effects of pre-existing stress on mechanical properties measured using nanoindentation including plastic and elastic indentations, a problem related to the transistor and thin film issues described above. In addition, a new atomistic thermostat based on coupling molecular dynamics simulation to the continuum heat equation will be presented. The goal of this thermostat is to

allow more accurate calculations of atomic scale friction forces of sliding interfaces by accurately modeling thermal transport properties, an issue important in the MEMS industry.

The remainder of this chapter will be dedicated to a discussion of molecular dynamics simulation, the energy function used in this work, a brief description of the computational method and algorithm used, and a description of the typical temperature control method used for most molecular dynamics simulations. This background will help give a clearer understanding of following chapters. In the second chapter, a general overview of nanoindentation will be given, including a historical background, important computational contributions, and a detailed description of the interpretation of data from a nanoindentation test including calculation of contact area, hardness, and indentation modulus. The third chapter presents the details of the set up of the molecular dynamics simulations used to simulate nanoindentation experiments. This includes a description of the system configuration, a description of two types of 'virtual' indenters and results of tests of these indenters.

In the fourth chapter, the relationship between pre-existing stress in the substrate material and indentation modulus is investigated. Due to anharmonicities in atomic interactions it is expected that the indentation modulus should very with pre-existing stress in the substrate. This had been used to explain the dependences observed in experiments in the past. However, Tsui, Pharr and Oliver[6] have shown in experiment and with finite difference calculations that the indentation modulus for indentations where plasticity is present is essentially independent of the pre-existing stress if the true contact area is used to make the

calculation. Their work showed that the dependence observed in the past was due to errors in the empirical estimates used to determine contact area from force-displacement curves. Their experiment is repeated using molecular dynamics simulation and the results of various empirical estimates for the contact area using force displacement curves have been compared to the true contact determined from the atomistic simulation. The results show that the empirical estimates lead to large errors in contact area and thus hardness and modulus are also in error. When true contact areas are used the results agree with experiment. Atomic level stress analysis is used to show that the pre-stress is relieved through plasticity induced by the indenter. This explains why the modulus is independent of the pre-stress level.

In the fifth chapter, by using shallow elastic indentations, it is shown that indentation can be used to predict the true dependence of pre-stress on the indentation modulus that is predicted by knowledge of the anharmonicity in the atomic potential. These results are compared to the second-order and third-order dependence of the bulk elastic constants in the material on the pre-stress level calculated using molecular statics methods. This comparison shows that the shallow elastic indentations predict the correct dependence of modulus on strain, although the magnitude of the dependence is somewhat smaller than predicted using the bulk elastic constants.

Somewhat removed from the preceding chapters, Chapter 6 presents a new method for temperature control in molecular dynamics simulations. In the simulation of metals, electronic interactions account for the majority of the heat flow. Mean field approaches such as the embedded atom method, which is presented below, do not account for electrons

explicitly and therefore thermal transport cannot be accurately modeled. To overcome this method, an *ad hoc* feedback between the molecular dynamics simulation and the continuum heat flow equation has been developed. The method relies on experimental values for the thermal conductivity and heat capacity as inputs for a finite difference solution to the continuum equation. A full description of the method is presented. The thermostat was tested for a simple quasi one-dimensional case and results are shown to be in excellent agreement with the analytical solution for one-dimensional heat flow. The method was extended to three dimensions and applied to the problem of substrate heating due to sliding of a rigid spherical tip. Although the temperature changes in the substrate due to the sliding tip are small, results show significant differences in the frictional force felt by the tip when the thermostat is turned on and off. The final chapter offers summary and conclusions to the work presented as well as a list of future research opportunities for both nanoindentation and the *ad hoc* thermostat.

1.2 Molecular dynamics simulation

Molecular dynamics is used to move atoms according to a model for interatomic potentials and to determine equilibrium energy structures. The atomic-scale dynamics are simulated by numerically integrating classical equation of motion, e.g. Newton's equation, for each atom,

$$F = ma \qquad \text{Eq. 1.1}$$

$$-\frac{dU}{dr} = m\frac{d^2r}{dt^2} \qquad \text{Eq. 1.2}$$

where U is the potential energy of the system, r and m are the atomic positions and mass of each atom, respectively, and t is time[7]. In our simulations the potential energy U is given

by an analytic expression that yields energy as a function of the relative positions of the atoms. The energy functional used in this work is known as the embedded atom method.

1.3 The embedded atom method

The selection of the embedded atom method (EAM) for the energy functional in molecular dynamics simulations is a popular choice for *fcc* close-packed metals[8-10]. It combines the computational simplicity required to model large systems with a physical picture that includes many-body effects and the moderation of bond strength by other bonds (coordination-dependent bond strength). With the EAM, the research community has investigated many problems of interest, including: point defects, melting, alloying, grain boundary structure and energy, dislocations, segregation, fracture, nanoindentation, surface structure, and epitaxial growth. In general, most of the EAM calculations have been carried out in close connection with experimental work.

Each atom in a solid can be viewed as an impurity embedded in a host material consisting of all the other atoms. Since the energy of the impurity depends on the electron density of the unperturbed host, the cohesive energy of the solid can be determined from the embedding energy. It is possible to obtain the electron density established by a given potential. The energy is then given as a function of that potential. This assumption alone leads to unrealistic properties of the solid, originating from an extreme locality or complete uniformity of the background. A real solid differs in that the charge densities are non-uniform. The energy function is corrected by taking an average density over a finite region

surrounding the impurity. An additional term is added to account for the core-core repulsion in the form of a pair-potential. This makes the EAM attractive computationally as it is relatively short-ranged and can be computed by summing over pair-wise interactions. In the EAM formalism the total potential energy U is taken as a sum of energies associated with each atom i given by

$$U_i = \sum_j \phi(r_{ij}) + F_{embed}\left(\sum_j \rho(r_{ij})\right) \qquad \text{Eq. 1.3}$$

where $\phi(r_{ij})$ is a core-core pair repulsion of atoms i and j at a radial distance of r_{ij}. F is an embedding function defined as the energy required to embed atom i in the electron density $\rho(r_{ij})$. This density is determined through a linear superposition of the surrounding j atoms. The ρ and F embedding functions are fit to various experimentally determined quantities such as equilibrium density, sublimination energy, elastic constants and vacancy formation energy. The core-core repulsion term $\phi(r_{ij})$ is based on a Coulombic potential with a parameterization that is derived from s and p electron densities as determined by Hartee-Fock wave functions.

1.4 PARADYN

PARADYN, a parallel implementation of the Daw's EAM code DYNAMO, is used for the MD simulations. PARADYN uses an algorithm developed by Plimpton[11] that utilizes force-domain decomposition to achieve N/√P scaling of computational time where N and P are the number of particles and processors. Each processor is assigned N/P atoms. The force

for all atoms can be described as an NxN force matrix, illustrated in FIG. 1.2, where element *ij* is the φ, ρ, or force interaction between atoms *i* and *j*. The total force on atom *i* is the sum of all elements in row *i* of the matrix. The matrix is sparse due to the short range nature of the interatomic forces and symmetric due to Newton's 3rd law. The algorithm is outlined below.

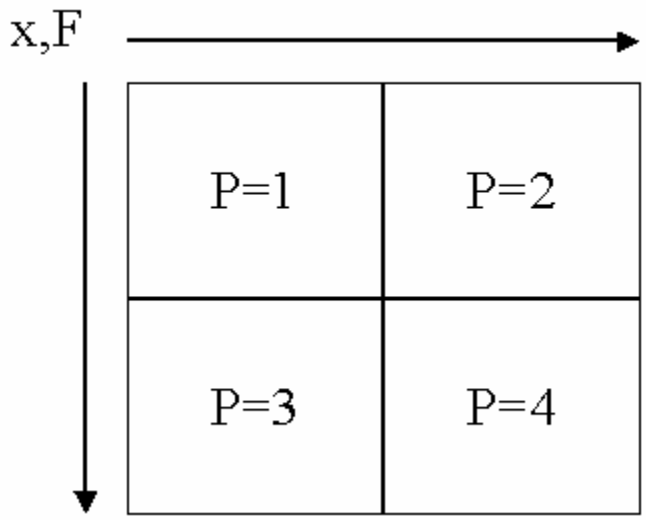

FIGURE 1.2: Processor assignment of the NxN force matrix. Each processor need only store two pieces of the position and embedding function vectors, each of length N/√P to compute the matrix elements. Processors then communicate this information along rows and columns.

For the system illustrated in FIG. 1.2:

1. Get N/√P positions of atoms in its row. (Proc 4 communicates with Proc 3.)
2. Transpose its N/P positions with appropriate processor (Proc 3 trades with 2)
3. Acquire N/√P positions of atoms in its column. (Proc 4 communicates with 2)
4. Calculate electron density matrix elements in each block.
5. Sum values across row (Proc 4 sums with 3)

6. Compute embedding functions (F and F') for each block of N/P atoms using summed density values.
7. Repeat the first 3 steps with F' instead of coordinates to get all the F' values for the N/√P atoms in its rows and columns of the matrix
8. Calculate the Force vectors in each block using F'.
9. Sum forces across rows and update positions.

These steps are easy to perform on a parallel machine. Communication takes place between small groups of √P processors and requires information exchange of length N/√P or shorter (versus length N for atom decomposition). Newton's 3rd Law can be used to halve the required communication. This is achieved by 'checker-boarding' the force matrix. This way each pair-interaction is only calculated once in the matrix.

1.5 The Nordsieck-Gear predictor-corrector algorithm

Given the molecular positions and their successive derivatives (velocity, acceleration, etc. at time t), molecular dynamics attempts to determine the positions, velocities, etc. at time $t+\delta t$ to some degree of accuracy[7]. By assuming that the classical trajectory is continuous, and that no forces act on the particles, the positions, velocities, accelerations, etc. at $t+\delta t$ can be estimated by Taylor series expansion.

$$\begin{aligned}
\mathbf{r}^{p}(t+\delta t) &= \mathbf{r}(t) + \delta t\mathbf{v}(t) + 1/2\,\delta t^{2}\mathbf{a}(t) + 1/6\,\delta t^{3}\mathbf{b}(t) + \ldots \\
\mathbf{v}^{p}(t+\delta t) &= \mathbf{v}(t) + \delta t\mathbf{a}(t) + 1/2\,\delta t^{2}\mathbf{b}(t) + \ldots \\
\mathbf{a}^{p}(t+\delta t) &= \mathbf{a}(t) + \delta t\mathbf{b}(t) + \ldots \\
\mathbf{b}^{p}(t+\delta t) &= \ldots
\end{aligned} \qquad \text{Eqs. 1.4}$$

The superscript *p* indicates 'predicted' values of position (**r**), velocity (**v**), acceleration (**a**) and higher derivatives. Unfortunately, Eqs. 1.4 will not predict the correct trajectories because the forces at each time step have not been taken into account. To get the corrected positions, etc., the new positions, $\mathbf{r}^p$, are used to calculate the force using the first derivative of the potential energy (i.e. Eq. 1.3) and hence the correct acceleration ($\mathbf{a}^c(t+\delta t) = \mathbf{F} / m$) at time $t+\delta t$ using the embedded atom formalism (or in principle any other formalism relating force to positional information). These values are compared to the predicted accelerations to estimate the error of the prediction step:

$$\Delta\mathbf{a}(t+\delta t) = \mathbf{a}^c(t+\delta t) - \mathbf{a}^p(t+\delta t) \qquad \text{Eq. 1.5}$$

The error and results from the predictor step Eqs. 1.4 and Eq. 1.5) are fed into the corrector step as follows:

$$\begin{aligned}
\mathbf{r}^c(t+\delta t) &= \mathbf{r}^p(t+\delta t) + c_0\Delta\mathbf{a}(t+\delta t) \\
\mathbf{v}^c(t+\delta t) &= \mathbf{v}^p(t+\delta t) + c_1\Delta\mathbf{a}(t+\delta t) \\
\mathbf{a}^c(t+\delta t) &= \mathbf{a}^p(t+\delta t) + c_2\Delta\mathbf{a}(t+\delta t) \\
\mathbf{b}^c(t+\delta t) &= \ldots
\end{aligned} \qquad \text{Eq. 1.6}$$

The values of $c_0, c_1, c_2 \ldots$ are chosen to optimize numerical stability and accuracy. These values for the Nordsieck-Gear[12,13] second order predictor-corrector using the first three derivatives of position are given in Table 1.1. While it is possible to iterate the predictor-corrector algorithm to achieve higher accuracy, the force calculation is the most time consuming part of simulation. Thus, a large number of predictor-corrector steps would be inefficient.

Table 1.1: Coefficient values for a second order Nordsieck-Gear[11,12] predictor-corrector using four values.

$c_0 = 1/6$	$c_1=5/6$	$c_2=1$	$c_3=1/3$

1.6 Temperature control

In the majority of the work presented in this thesis temperature control is achieved via the Generalized Langevin Equation (GLE)[14]. Based on the theory of Brownian dynamics[15], this technique assumes that the energy of single particles is exchanged with the remainder of the system in two ways. The first is friction, which models the dissipation of energy into the bulk. The second is by a fluctuating force, which mimics the thermal vibrations of the surrounding atoms. The two balance each other out and produce the desired average. The equation of motion, which describes these processes, is given by

$$m\frac{d\mathbf{v}}{dt} = -m\beta\mathbf{v} + \mathbf{F} \qquad \text{Eq. 1.7}$$

where m and $\mathbf{v}$ are the mass and velocity of the particle, β is a generalized friction coefficient and $\mathbf{F}$ is a random force. The random forces used in the Generalized Langevin Equation have a Gaussian distribution centered about zero given by

$$\mathbf{F} = \sqrt{\frac{2\beta k_B T}{dt}}\mathbf{R}_{Gauss}$$

where β is a constant derived from the Debye frequency, k_B is Boltzmann's constant, T is the desired temperature, dt is the time step size, and $\mathbf{R}_{Gauss}$ is a random number with a Gaussian distribution given by

$$R_{Gauss} = \sqrt{-2\log(R_1)}\cos(2\pi R_2)$$

where R_1 and R_2 are randomly generated numbers between 0 and 1. In PARADYN the opposing frictional term βv and the random force F are added to the total force before the correction step in the integrator. PARADYN uses a value of 0.1 for β. The distribution width of the Gaussian sets the desired temperature.

1.7 References

1. R. Feynman, "There's plenty of room at the bottom," talk given to the American Physical Society, Dec. 29, 1959 at Cal. Tech.

2.see INTEL's research website, http://www.intel.com/research/silicon/nanometer.htm

3. Bhushan, B., *Principles and Applications of Tribology*, John Wiley, New York, 1999.

4. V. Yanakov, D. Wolf, S.R. Phillpot, A.K. Mukherjee, and H. Gleiter, "Deformation mechanism crossover and mechanical behavior in nanocrystalline materials", *Phil. Mag. Letts., 83, 2003, 385.*

5. W.R. LaFontaine, C.A. Paszkiet M.A. Korhonen, and Che-Yu Li, *J. Mater. Res.* 6, 1991, 2084.

6. T.Y. Tsui, W.C. Oliver, and G.M. Pharr, "Influences of stress on the measurement of mechanical properties using nanoindentation: Part I. Experimental studies in an aluminum alloy", *J. Mater. Res*. 11, 1996, 752.

7. Allen, M.P. and D.J. Tildesley *Computer Simulations of Liquids*. Clarendon Press, Oxford 1987.

8. M.S. Daw and M.I. Baskes, "Embedded-atom method: derivation and application to impurities, surfaces, and other defects in metals." *Phys Rev B.* 29, 1984, 6443.

9. S.M. Foiles, M.I. Baskes, and M.S. Daw, "Embedded atom method functions for the FCC metals Cu, Ag, Au, Ni, Pd, Pt, and their alloys.", Phys. Rev. B. 33, 1986, 7983.

10. M.S. Daw, S.M. Foiles, M.I. Baskes, "The embedded atom method: a review of theory and applications." Materials Science Reports, 9, 1993, 251.

11. S.J. Plimpton and B.A. Hendrickson, "Parallel Molecular Dynamics with the embedded atom method," *Mat. Res. Soc. Symp. Proc*., 291, 1993, 37.

12. Gear, C.W. *Numerical initial value problems in ordinary differential equations.* Prentice-Hall, Englewood Cliffs, NJ, 1971.

13. A. Nordsieck, "On numerical integration of ordinary differential equations." *Math Comp.*, 20, 1962, 130.

14. R. Kubo, "Fluctuation-dissipation theorem" *Rep. Prog. Theor. Phys.* 33, 1965, 425.

15. D. A. McQuarrie, *Statistical Mechanics*. Harper and Row, New York, 1976.

2. INTRODUCTION TO NANOINDENTATION

The history of indentation as a means to determine materials properties is long and rich. Hertz and Boussinesq first considered the elastic contact problem in the 1880's[1]. Boussinesq developed a means of computing the stresses and displacements in an elastic body loaded by a rigid indenter. Hertz investigated elastic contact between two spheres with different radii and elastic constants. Their work forms the basis for the majority of experimental and theoretical studies in contact mechanics since.

2.1 Historical Background

In 1900, Brinnell began to investigate indentation of metals by large spherical indenters (macroindentation). He was interested in comparing various steels and thought that indentation might prove to be an alternate to the uniaxial tensile test. He showed that a material's resistance to indentation, also known as hardness - which he defined as peak load over the area of indention - was a good measure of the steel's resistance to mechanical deformation. Several other developments also occurred early in the 20^{th} century. The first was the concept of critical resolved shear stress[2]. It was found in uniaxial tests that below this critical value of stress all deformation is elastic and recoverable. Above this limit, permanent plastic deformation occurs. The second advance was the explanation of plastic deformation in terms of dislocations[3-5]. This also explained observations of increasing yield stress with increasing amounts of strain, i.e. work hardening. Tabor used these developments to formulate the well known expression that states that hardness is

approximately equal to three times the critical resolved shear stress and showed that it is a surprisingly good estimate for heat-treated plain carbon steels and medium alloy steels[6]. Tabor also showed that this expression holds for conical and pyramidal indenters as well[7]. In principle, hardness does not depend on the size of the indention for such indenters. Atkins and Tabor also observed that indentions relax elastically upon unloading and thus can be put in terms of Hertz's elastic equations[8]. These equations were then modified and used to calculate the elastic modulus from an indentation experiment. Indention testing offered significant advantages over uniaxial testing. It was no longer necessary to fabricate large tensile specimens and analysis of very small and very thin samples was possible. In the 1960's, large steel spherical indenters were supplanted by small pyramidal diamond indenters, allowing indentations on the order of microns[9]. These 'microindentation' tests were capable of probing the deformation properties of grain boundaries, different phase regions, and local work hardening. This trend in miniaturization of probe size continues today, in the form of nanoindentation testing.

In the last twenty years, refinements in instrumentation have allowed probes to measure materials properties at the nanoscale[10]. This trend has been driven chiefly by the technological need to know mechanical properties in semiconductor devices as well as thin films and coatings. The key development has been continuous monitoring of displacement and load during the indentation. In principle, load-displacement data can then be used to derive properties without actual direct measurement of the contact area, which is difficult to obtain due to the small size of the indentations. Information from nanoindentation can be mapped to various microscopy techniques such as atomic force microscopy, scanning electron microscopy,

x-ray topography, etc. to form a unique understanding of the relationship between mechanical properties and various phases, structures, and defects at the nanoscale[11].

2.2 Important computational contributions

In many cases, an exact atomistic representation of the mechanisms leading to the data obtained through nanoindentation remains unclear making interpretation of nanoindentation data difficult. As a result, the problem of nanoindentation has been the focus of a number of atomistic studies. Tadmor and coworkers developed a quasi-continuum method capable of representing very large system sizes and used this model to predict the resolved shear stress required for emission of a dislocation dipole[12]. Their work also led to important insights into the onset of plastic deformation, dislocation nucleation, and dislocation image forces due to nanoindentation. However, these calculations were based on an idealized two dimensional model which limits its ability to be compared to experiment. A number of workers have applied the embedded atom method to model nanoindentations. In 1990, Landman and coworkers studied the influences of repeated contact[13]. While limited in size, their work was useful in explaining the 'jump-to-contact' phenomena observed in experiment. More recently indention simulations by workers such as Kelchner[14], Zimmerman[15], Rodriguez[16], and Lilleodden[17,18] have achieved length scales approaching that of experiment. These simulations have used the embedded atom method along with an energy minimization scheme to explore the issues of onset of plasticity, dislocation nucleation and various structural effects such as of surface steps and grain boundaries. Zimmerman and Kelchner [15] also developed a parameterization that allows dislocations and other defects in the simulated material to be easily visualized and characterized.

2.3 The nanoindentation test

As mentioned above, the nanoindentation test relies on the continuous monitoring of force and displacement as the indenter penetrates the sample. The resulting force-displacement curves are used to determine the mechanical properties, most typically hardness and elastic modulus[19]. A schematic diagram of a typical force-displacement curve is shown in FIG 2.1. Hardness is normally defined as a mean pressure P_m given by

$$P_m = \frac{P_{\max}}{A} \qquad \text{Eq. 2.1}$$

where P_{max} is the maximum load or force during an indentation cycle while A is the projected area of the indentation at the maximum load. The reduced modulus E_r is given by

$$E_r = \frac{S}{2}\sqrt{\frac{\pi}{A}} \qquad \text{Eq. 2.2}$$

where S is the unloading stiffness or initial slope of the unloading curve, and A again is the projected contact area at maximum load[9]. The reduced modulus is defined as

$$\frac{1}{E_r} = \frac{(1-\upsilon_s^2)}{E_s} + \frac{(1-\upsilon_i^2)}{E_i} \qquad \text{Eq. 2.3}$$

where υ_s, υ_i and E_s, E_i are Possion's ratio and modulus of the sample and indenter respectively. While a value for S can be obtained easily from experimental force-displacement curves as indicated in FIG. 2.1, the projected area during indentation cannot be easily measured.

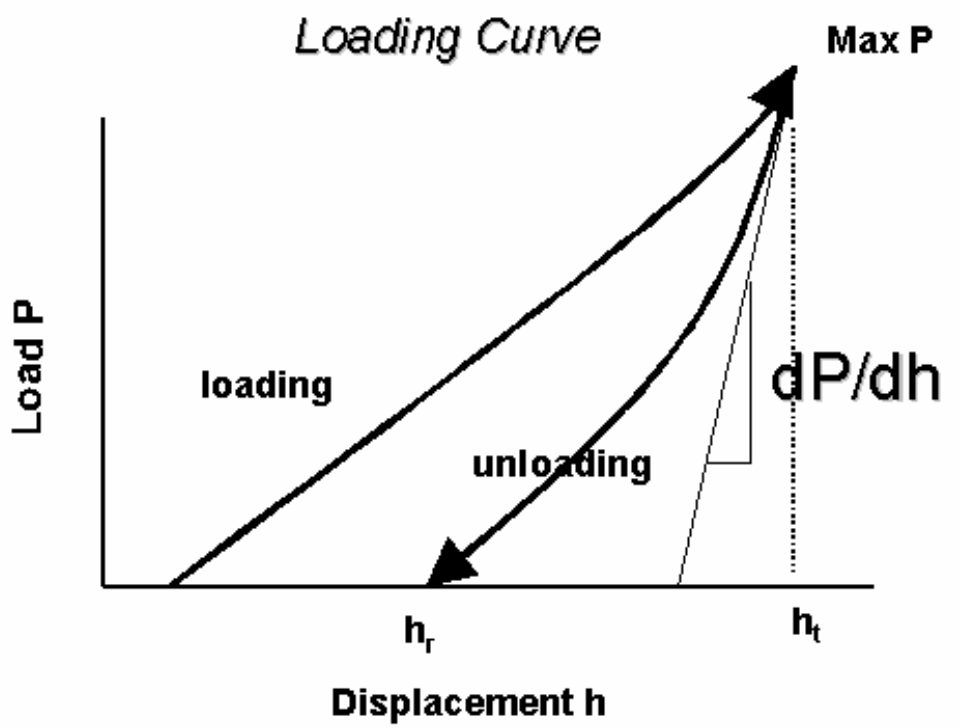

FIGURE 2.1: Schematic diagram of a load versus displacement curve for loading and unloading. Max P is load at maximum displacement h_t. Residual plastic deformation is given by h_r. The unloading stiffness is given by the slope of the unloading curve dP/dh at maximum displacement.

In experiments, typically either the dimensions of a remaining impression are measured optically after unloading, a finite element calculation is used to estimate contact area, or an empirical calculation is made. For the latter the projected area of contact is typically estimated using an empirically determined shape function $A = f(h_p)$, where h_p is defined as the depth of plastic contact. Several methods with varying degrees of accuracy have been proposed. Field and Swain suggested a very crude model for spherical indenters based solely on geometrical considerations [20]. To a first approximation, the depth of plastic contact h_p may be estimated as

$$h_p = \frac{h_t + h_r}{2} \qquad \text{Eq. 2.4}$$

where h_t is the maximum displacement and h_r is the depth of the residual impression after the load is removed. We will refer to this approximation in the remainder of the paper as the Field and Swain (FS) method. In the case of a spherical indenter of radius R, the depth of plastic contact is then used to estimate the radius of contact a of the indenter

$$a = \sqrt{2Rh_p - h_p^2} \qquad \text{Eq. 2.5}$$

The projected contact area is given as $A=\pi a^2$. In 1992, Oliver and Pharr proposed a more robust approximation that accounts for the curvature of the unloading curve and provides a physically justifiable estimation for the depth of plastic contact [19]. In this classic model, the depth of plastic contact is given by

$$h_p = h_t - \varepsilon \frac{P_{\max}}{S} \qquad \text{Eq. 2.6}$$

where again h_t is the maximum displacement, P_{max} is the maximum load and S is the unloading stiffness. The constant ε is a geometrical factor related to the deflection of the surface at the contact perimeter that depends on the indenter geometry. For a shallow indentation with a spherical indenter ε is equal to that of a parabola of revolution or 0.75. This approximation will be referred to as the OP method. For a parabola of revolution or spherical indenter, h_p may be substituted into Eq. 2.5 to determine the radius of contact and thus the projected contact area A.

2.4 References

1. D. Tabor, *The hardness of metals*, Oxford University Press, London, 1951, and references contain with in.

2. E. Schmid, *Z. Elektrochem*, 37, 1931, 447.

3. G.I. Taylor, *Proc. R. Soc. Londo*n, 145A, 1934, 362.

4. E. Orowan, *Z. Phys*., 89, 1934, 605.

5. M. Polanyi, *Z. Phys*., 89, 1934, 660.

6. D. Tabor, "Indentation hardness", *Proc. R. Soc. A* 192, 1942, 247.

7. N.A. Stilwell and D. Tabor, "Determining the strain exponent from indentation hardness", *Proc. Phys. Soc*. 78, 1961, 169.

8. A.G. Atkins and D. Tabor, "Indentation measurements and elastic properties", *Mech. Phys. Solids* 13, 1963, 149.

9. H. Buckle, "Microindentation measurements of thin films", *Metall. Rev*. 4, 1959, 49.

10. *see for instance* J.B. Pethica, R. Hutchings, W.C. Oliver, "Hardness measurement at penetration depths as small as 20nm", *Philo. Mag. A* 48, 1983, 593.

11. *see for instance* S.A. Joyce, J.E. Houston, "A new force sensor incorporating force-feedback control for interfacial force microscopy", *Rev. Sci. Instrum*. 62, 1991, 710.

12. E.B. Tadmor, R. Miller, and R. Phillips, "Nanoindentation and incipient plasticity," *J. Mater. Res*., 14, 1999, 2233.

13. U. Landman, "Atomistic mechanisms and dynamics of adhesion, nanoindentation and fracture," *Science*, 248, 1990, 454.

14. C.L. Kelchner and S.J. Plimpton "Dislocation nucleation and defect structure during surface indentation," *Phys Rev B.,* 58, 1998, 11085.

15. J.A. Zimmerman, , C.L. Kelchner, , P.A. Klein, J.C. Hamiltion, and S.M. Foiles, "Surface Step Effects on Nanoindentation" *Phys. Rev. Letts*. 87, 2001, 165507.

16. O. Rodriguez de Fuente, J.A. Zimmerman, MA Gonzalez, J. de la Figuera, J.C. Hamilton, Woei Wu. Pai, J.M. Rojo. "Dislocation emission around nanoindentations on (001) fcc metal surface studied by scanning tunneling microscopy and atomistic Simulations", *Physical Review Letters*. 88, 2002, 36101.

17. E.T. Lilleodden, PhD thesis: *Indentation-Induced plasticity of thin metal films*, Stanford University, 2001.

18. E.T. Lilleodden, J.A. Zimmerman, S.M. Foiles and W.D. Nix, "Atomistic Simulations of Elastic Deformation and Dislocation Nucleation During Nanoindentation", *J. Mech. Solids*, 51, 2003, 901.

19. W.C. Oliver and G.M. Pharr, "An improved technique for determining hardness and elastic modulus using load and displacement sensing indentation experiments," *J. Mater. Res.* 7, 1564, 1992.

20. J.S. Field "A simple predictive model for spherical indention," *J. Mat. Res*. 8, 1993, 297.

3. MOLECULAR DYNAMICS SIMULATION OF INDENTATION

The following chapter gives an overview of the techniques used to conduct molecular dynamics simulation of nanoindentation given in Chapters 4 and 5. The first section shows the simulation setup and lists parameters for the simulated material. The next two sections discuss a repulsive potential and rigid indenter. The last section presents a series of tests of the indenters.

3.1 Simulation set-up

The molecular dynamics code *Paradyn* developed by Plimpton[1] was used to model the indentation gold surfaces. *Paradyn* utilizes embedded-atom method potentials such as those developed by Foiles, Daw, and Baskes[2] to model atomistic behavior of *fcc* and other close-packed metals. For such materials, the embedded atom formalism has proven to be particularly good at modeling bulk and defect properties such as energies and structures and has been used extensively to model the onset of plasticity during the nanoindentation of gold in quasi-static (0 temperature) simulations and to a smaller extent with molecular dynamics (nonzero temperature). The materials constants derived from the Au potential used in this study are given in Table 3.1. A crystal lattice was generated by tessellating a unit cell with the desired crystallographic orientation by a desired number of repeat units in the x, y, and z directions. The majority of the simulations conducted in this work were oriented such that there was a <111> direction normal to the free surface. A schematic diagram of the model used in the simulated indentation tests is shown in FIG. 3.1. In the figure the z direction is

taken to be the normal to a {111} plane. The *x* axis is taken to be along a <110> close-packed direction and *y* is along a <112> direction. The bottom layer of atoms is held rigid in the z-direction and the sides are maintained through periodic boundaries in the x and y directions.

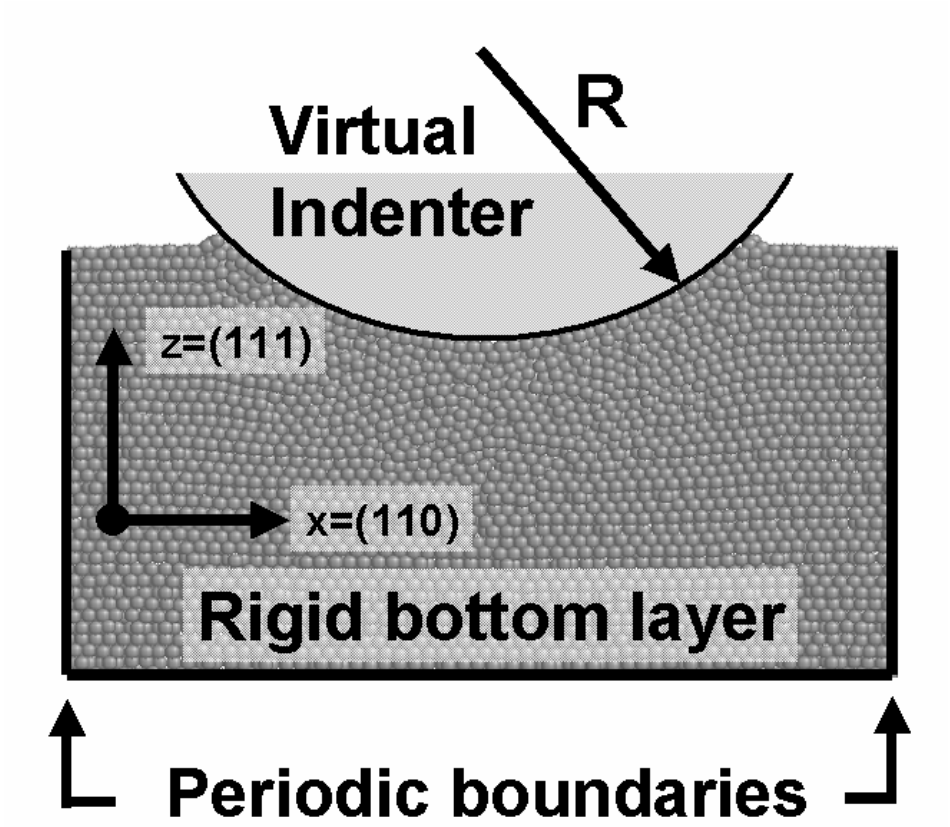

FIG. 3.1. Schematic diagram of the setup for the molecular dynamics simulation. The x axis is along a <110> direction, the z axis is oriented in the <111> direction, and y axis forms a right-hand coordinate system along a <112> direction (normal to the plane of the illustration). Periodic boundaries are held in the x and y directions. The bottom layer of atoms is held rigid. R is the radius of the virtual indenter.

Table 3.1: Materials properties of gold derived from the embedded atom potential as reported by Foiles, Daw, and Baskes [2]: equilibrium lattice constant, bulk modulus, cohesive energy, vacancy formation energy, and elastic constants. 1 nN/Å^2 is equivalent to 100 GPa.

a_o	4.08 Å	C_{11}	1.83 nN/Å^2
B	1.67 nN/Å^2	C_{12}	1.59 nN/Å^2
E_{coh}	3.93 eV	C_{44}	0.45 nN/Å^2
E_v^f	1.03 eV		

3.2 Repulsive potential indentation

In the next two sections, two types of so called 'virtual' indenters will be discussed. The first relies on a repulsive potential to generate atomic displacements by the indenter. The second simply displaces the atoms rigidly in a manner that describes the geometry of the indenter. In the repulsive potential formulation for the virtual indenter, the indenter acts as if it were a 'giant' atom with a repulsive force between the indenter and atoms the indenter contacts. The force from the indenter *I* on substrate atom *i* is given as

$$F_i = 0 \text{ for } r_{iI} \geq R$$
$$F_i = -k(R - r_{iI})^n \text{ for } r_{iI} < R \qquad \text{Eq. 3.1}$$

where *R* defines the radius of a 'virtual' spherical indenter, r_{iI} is the radial distance from the center of the indenter to atom *i*, and *n* and *k* are constants related to the stiffness of the indenter, see FIG 3.2. A strictly repulsive interaction, which is similar to other recent simulations, is intended to mimic non-adhesive contact[3-7]. The total force on atom *i* is then:

$$F_i = F_{EAM} + F_{iI} \qquad \text{Eq. 3.2}$$

where F_{EAM} is the total force determined by the embedded atom method and F_{iI} is the force on atom i from the indenter. To simulate loading or unloading of the indenter, the center of the indenter is placed above the substrate in preparation for the indention. Typically it is centered in x and y with respect to the periodic boundaries of the system. The z component for the center of the indenter is then given as the maximum z coordinate of the substrate atoms plus the radius of the indenter plus some small increment of displacement. This initial placement of the indenter ensures that the indenter is not in contact with the surface at the start of the simulation. To load or unload the substrate, the z coordinate of the indenter is decreased or increased by I_{depth} / n_{steps} at each molecular dynamics time step where n_{steps} is the number of time steps required to indent to a depth of I_{depth}. Similarly the indenter may be rastered across the surface by changing the x and y coordinates of the indenter center. The force on the indenter is then calculated by summing the forces normal to the surface for all atoms in contact with the indenter ($r_{iI} < R$). The force data along with the displacement of the indenter are used to generate force-displacement curves.

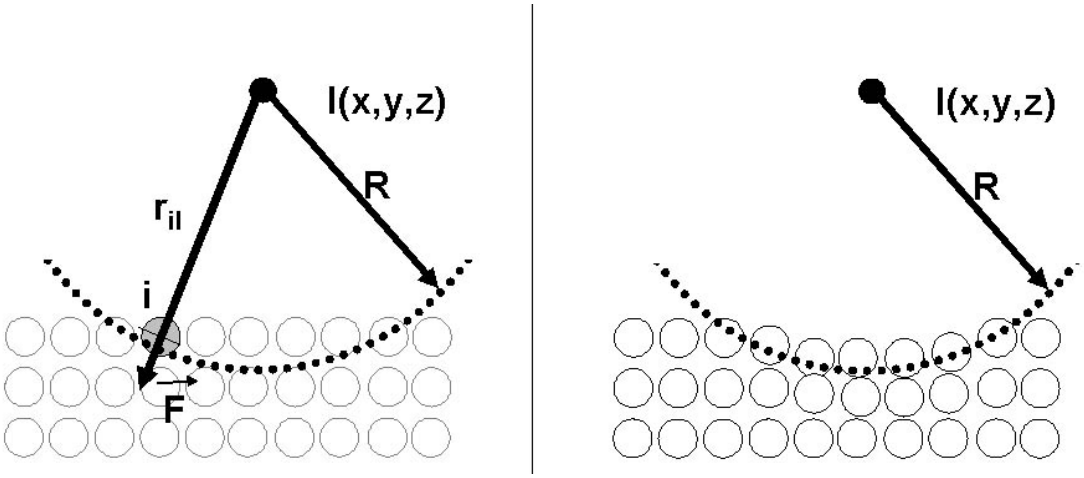

FIGURE 3.2: Schematic diagram of the repulsive potential indenter. A normal force is applied normal to the surface of the indenter (left panel). The actual displacement of atoms in contact with the indenter depends on the constants in Eq. 3.1

3.3 Rigid Indentation

Placement of the rigid indenter is identical to that of the repulsive potential indenter. However, instead of adding a force, a rigid displacement of contacted atoms is made. At each step the magnitude of the radial vector $\mathbf{V}_j$ between the coordinate of atom $\mathbf{A}_j$ and the indenter position $\mathbf{I}(x,y,z)$ is calculated $\mathbf{V}_j = \mathbf{I} - \mathbf{A}_j$. Contact between atoms and the indenter is defined as follows: For $|\mathbf{V}_j| < R$ where R is the radius of the indenter, the atom in contact and the atom is moved along the radial vector $\mathbf{V}_j$ to the point where $|\mathbf{V}_j| = R$. This generates a rigid displacement of atoms by the indenter that exactly matches the geometry of the indenter; see the illustration in FIG 3.3. The atom is made rigid by zeroing its velocity, acceleration, and higher order derivatives so that the shape of the contact is maintained, i.e atoms cannot move back inside the indenter. Once an atom loses contact with the indenter,

for instance during unloading, it is no longer constrained. For $|\mathbf{V}_j| > R$ there is no contact. This type of indenter gives a more accurate estimate of the elastic properties of the material being indented; however, it works only for loading. During unloading, atoms loose contact with the indenter and no force is registered.

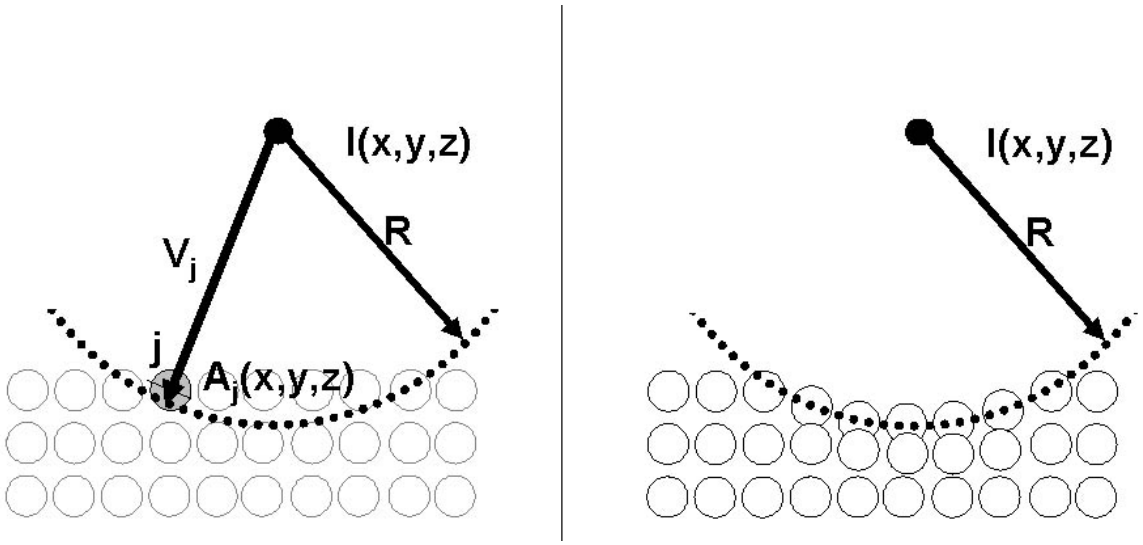

FIGURE 3.3: Schematic diagram of the rigid indenter. Atoms are rigidly displaced normal to the surface of the indenter such that |**V**j| = R.

3.4 Tests and comparisons of the indenter functions

Lilleodden *et al* [6,7] have spent considerable effort in understanding indenter stiffness on the 'virtual' indenter function expressed by Eq. 3.1. In their work they settled on values of *n* and *k* to be 2 and 10 eV/Å^3 , respectively. As a point of reference 1 eV/Å^3 equals 160 N/m^2. Lilleodden utilized a conjugate gradient energy minimization scheme to determine the equilibrium structure at each indentation displacement before moving to the next. This is equivalent to indenting at a very slow indentation rate but at zero temperature. Molecular

dynamics simulations were performed only at specific points along the force-displacement curve where dislocation emission occurred as indicated by discontinuities in the force-displacement curves. In our simulations we have chosen to simulate the entire indentation cycle using molecular dynamics. Due to the computational limitations inherent to molecular dynamics simulations, namely that of time-scale, the trade-off of this choice is a high indention rate. The particles in each simulation are held at the thermal equivalent of 300 K via the generalized Langevin equation thermostat[8]. For a typical indention simulation of gold, a molecular dynamics time step of 0.005 ps was used. At each time step the indenter is moved 0.01 Å down or up for loading or unloading. This results in an indentation rate of 2 Å/ps. Although much faster than experimental indentation rates, which are on the order of Å/s, the indention rate in our simulations is still approximately eight times slower than the theoretical dislocation velocity in bulk gold. As a result the underlying plastic deformation mechanisms are largely independent of the indentation rate with the benefit that any thermally activated processes present in a typical indentation experiment may be accurately represented. We conducted several small test cases to qualify the indenter function. The results are significantly different than those reported by Lilleodden and others for simulations using conjugate gradient minimization schemes and led us to the selection of different values for the indenter stiffness parameters n and k. Illustrated in FIG. 3.4a are the force-displacement curves of several small scale molecular dynamics simulations of indention with varying values of the constant k at a constant value $n = 1$. A 10 Å radius indenter was used to indent a (111) oriented substrate with dimensions 70 Å x 70 Å x 70 Å to a depth of 5 Å at a constant displacement rate of 2 Å /ps. Small values of k (>0.5 eV/Å^2) suggest an overly compliant indenter which leads to little or no plastic deformation of the substrate. Large

values of k (> 5 eV/Å^2) cause bouncing of the atoms as they make and lose contact with the tip. This leads noisy data making analysis difficult. Shown in FIG. 3.4b are force-displacement curves of the same substrate with varying values for the exponent n with a constant $k = 1$ eV/Å^{n+1}. Over the range of n evaluated no one value appears to be better than another.

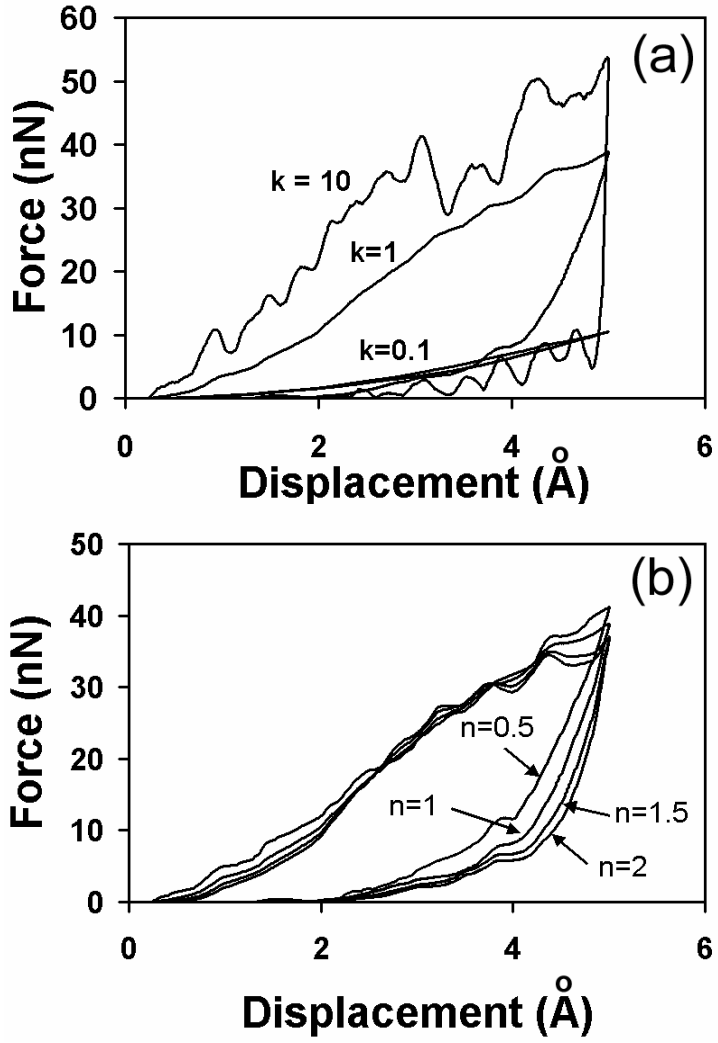

FIGURE 3.4. Force-displacement curves for (a) varying values of the constant k with $n = 1$, and (b) for varying values of the constant n with $k = 1$.

Based on these tests we have found suitable values of n and k in Eq. 3.1 to be 1.0 and 1.0 eV/Å^2, respectively. For the range of indenter stiffness parameters tested it does not appear possible to back calculate a value for the modulus or Poisson's ratio of the indenter, a problem also noted by Lilleodden[6]. Therefore all modulus values reported are for reduced modulus instead of the substrate modulus.

Finite element simulations by several other groups have reported observable periodic boundary effects for substrate thicknesses less than 50 times the indention depth[9,10]. To determine the effect of the rigid boundary layer on indentation results in our simulations, three substrates with thicknesses of 63, 126 and 190 Å were indented to a maximum depth of 20 Å with a 100 Å radius indenter. The x and y dimensions were held constant at 300 Å and 300 Å for each substrate indented. The simulated force-displacement curves are shown in FIG. 3.5.

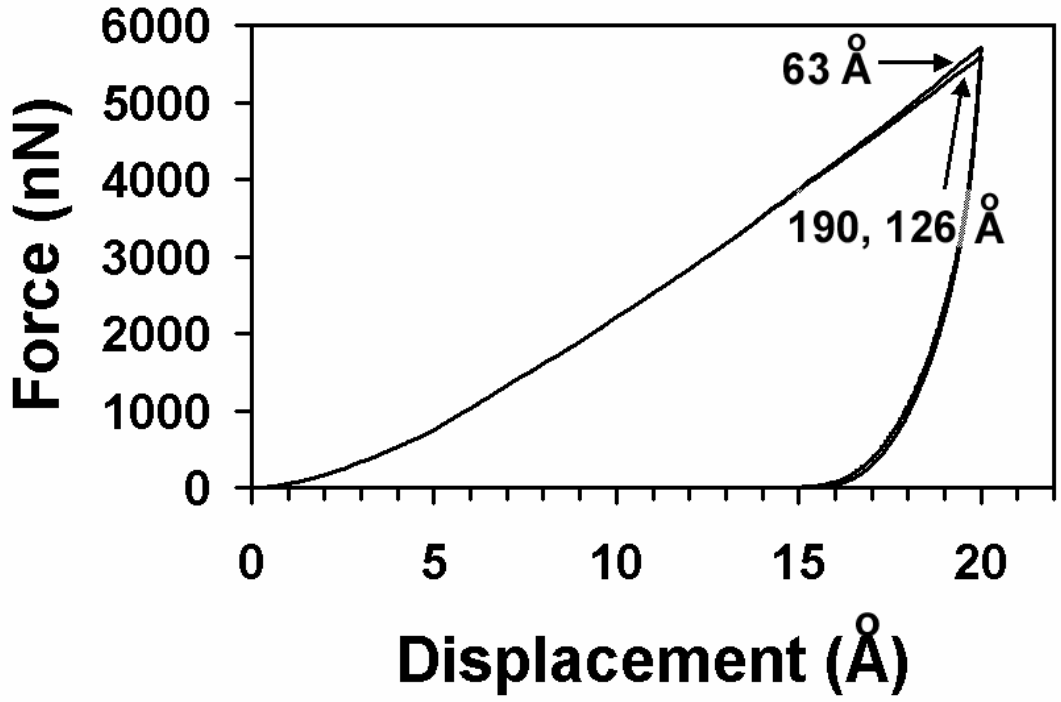

FIGURE 3.5. Force-displacement curves for substrate thicknesses of 63, 126 and 190 Å indented to a depth of 20 Å with a 100 Å radius indenter. The curves overlap completely for the 126 and 190 Å thick substrates with only a slight increase in the force with displacement for the 63 Å substrate with respect to the other substrates.

Only minor differences were observed. The force-displacement curves for the 190 and 126 Å thick substrates overlap completely while the 63 Å thick substrate shows only a slight increase in the force with displacement over the 190 and 126 Å substrates. This translates into an increase in hardness of only 2% and a negligible change in the reduced modulus. These results are consistent with the finite element simulations of soft thin-films on hard substrates conducted by Chen and Vlassak [11]. They observed that film thickness effects only have significant importance for indent depths greater than 50% of the film thickness. Our current computational resources limit us to simulations consisting of roughly one million atoms. This corresponds to a substrate size of approximately 300 Å x 300 Å x 190 Å. We

limited the indentation depth to 20 Å or approximately 10% of the substrate thickness. Additional analysis of atomic stresses during indentation showed that the in-plane periodic boundary conditions *x* and *y*) do not influence the results significantly.

Consider the equation for the reduced modulus

$$\frac{1}{E_r} = \frac{(1-\upsilon_s^2)}{E_s} + \frac{(1-\upsilon_i^2)}{E_i}$$

first given in section 2.3. The repulsive potential indenter does not allow accurate calculation of the substrate modulus because the indenter modulus E_i is indeterminate. For the rigid indenter, E_i goes to infinity, and therefore

$$\frac{1}{E_r} = \frac{(1-\upsilon_s^2)}{E_s} \qquad \text{Eq. 3.3}$$

giving an expression for the reduced modulus that does not include the modulus of the indenter. The rigid indenter does not allow for unloading so the equation in effect making the stiffness in the equation

$$E_r = \frac{S}{2}\sqrt{\frac{\pi}{A}}$$

go to infinity. The solution lies in the Hertzian analysis. This relation assumes a linear-elastic relation between the indenter and the surface, i.e. no plasticity and no adhesion. If this requirement is met, the relationship between load and deformation closely follows the Hertzian model for a rigid, non-interacting parabolic punch deforming an elastic half space which can be expressed as a power law expression

$$P = \frac{4}{3} E_R \sqrt{R} d^{3/2} \qquad \text{Eq. 3.4}$$

where P is the applied load, R is the radius of the indenter, and d is the depth of the indentation. If the initial portion of the force-displacement curve is fit to this equation, a direct measure of the elastic response of the material is possible. The simplest way to make the fit is by taking the natural log of Eq.3.4.

$$\ln P = 3/2 \ln d + \ln\left(\frac{4}{3} E_r \sqrt{R}\right) \qquad \text{Eq. 3.5}$$

which is simply the equation for a straight line ($y = mx + b$). Given the radius R of the indenter, it is straight forward to solve for the reduced modulus E_r. An example force displacement curve for a <001> oriented substrate is shown in FIG. 3.6a. The sample was indented to a depth of 2.5 Å at a rate of 0.5 Å/ps with a 40 Å radius indenter. No plastic damage was observed. The rigid indenter creates singularities in the force as individual atoms come in contact with the indenter. It also incorporates the random frictional forces that are imposed by the GLE thermostat. As a result, the data appears quite noisy compared to the force-displacement curves shown in FIGS. 3.4 and 3.5 for the repulsive potential indenter. To generate good data from the noise a running average with a 21 point centered spread is calculated. The results of this averaging and fitting to a ln-ln plot are shown in FIG 3.6b.

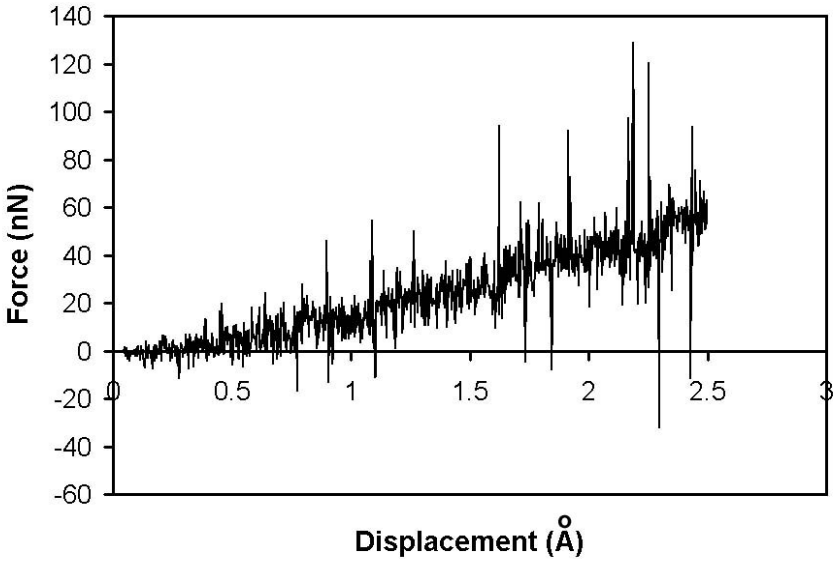

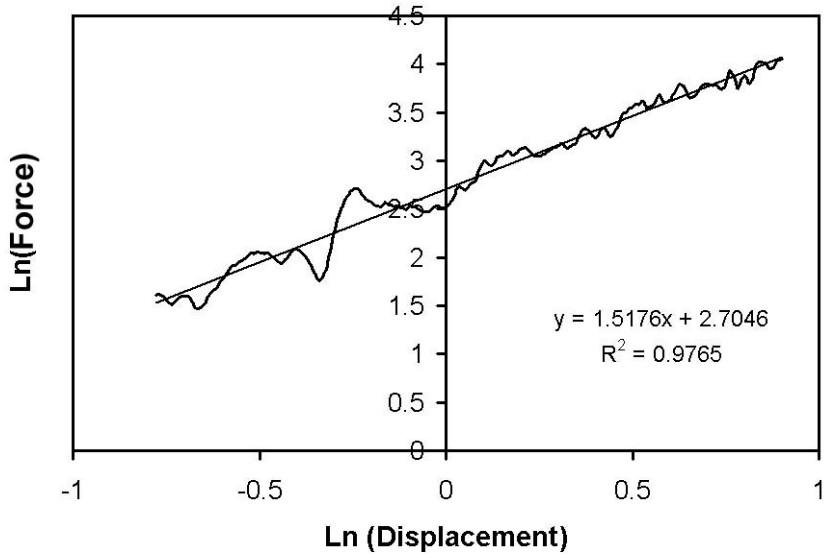

FIGURE 3.6: Force displacement curves for a <001> oriented substrate indented to 2.5 Å at a rate of 0.5 Å/ps with a 40 Å radius indenter. a) Raw force-displacement data, b) smoothed ln-ln data and linear fit.

The linear fit to the data shown in FIG. 3.6 yields a value for the exponential of 1.52 which is in very good agreement with the Hertzian exponent value of 1.5 as seen in Eq. 3.4. Calculating the modulus with the intercept value of 2.70 and the indenter radius of 40 Å gives an indentation modulus of 1.77 nN/Å^2 (177 GPa). This value is in reasonably good agreement

(order of magnitude) with the value of 0.55 nN/Å^2 (55 GPa) for the indentation modulus of bulk EAM gold obtained using the elastic constants given in Table 3.1. When considering the twelve order of magnitude difference in the indentation rates between simulation and experiment, this order of magnitude agreement is remarkable. More detailed calculations of the indentation modulus using the rigid indenter will be given in Chapter 5.

3.5 References

1. S.J. Plimpton and B.A. Hendrickson, "Parallel Molecular Dynamics with the embedded atom method," *Mat. Res. Soc. Symp. Proc*., 291, 1993, 37.

2. S.M. Foiles, M.I. Baskes, and M.S. Daw, "Embedded atom method functions for the FCC metals Cu, Ag, Au, Ni, Pd, Pt, and their alloys.", Phys. Rev. B. 33, 1986, 7983.

3. C.L. Kelchner and S.J. Plimpton "Dislocation nucleation and defect structure during surface indentation," *Phys Rev B.,* 58, 1998, 11085.

4. J.A. Zimmerman, , C.L. Kelchner, , P.A. Klein, J.C. Hamiltion, and S.M. Foiles, "Surface Step Effects on Nanoindentation" *Phys. Rev. Letts*. 87, 2001, 165507.

5. O. Rodriguez de Fuente, J.A. Zimmerman, MA Gonzalez, J. de la Figuera, J.C. Hamilton, Woei Wu. Pai, J.M. Rojo. "Dislocation emission around nanoindentations on (001) fcc metal surface studied by scanning tunneling microscopy and atomistic Simulations", *Physical Review Letters*. 88, 2002, 36101.

6. E.T. Lilleodden, PhD thesis: *Indentation-Induced plasticity of thin metal films*, Stanford University, 2001.

7. E.T. Lilleodden, J.A. Zimmerman, S.M. Foiles and W.D. Nix, "Atomistic Simulations of Elastic Deformation and Dislocation Nucleation During Nanoindentation", *J. Mech. Solids*, 51, 2003, 901.

8. R. Kubo, "Fluctuation-dissipation theorem" *Rep. Prog. Theor. Phys.* 33, 1965, 425.

9. A. Bolshakov, W.C. Oliver and G.M. Pharr, J. Mater. Res. 11, 1996, 760.

10. G.M. Pharr and A. Bolshakov, J. Mater. Res., 17, 2002, 2660,.

4. THE INFLUENCE OF PRE-EXISTING STRESS ON THE INTERPRETATION OF NANOINDENTATION DATA – PLASTIC INDENTATION

By using molecular dynamics simulations the true contact area during plastic indentation of materials under an applied in-plane stress has been determined. It has been observed that the mean pressure calculated from the true contact area varies slightly with applied pre-stress, with higher values in compression than in tension, and that the modulus calculated from the true contact area is essentially independent of the press-stress level in the substrate. These findings are largely consistent with the findings of Tsui, Pharr, and Oliver [1]. On the other hand, if the contact area is estimated from approximate formulae, the contact area is under-estimated and shows a strong dependence on the pre-stress level. When used to determine mean pressure and modulus, the empirically determined area leads to large errors. These simulations demonstrate that this phenomena, first reported for macro-scale hardness measurements dating back to 1932[2], also exists at the nanometer-scale contact areas, apparently scaling over 10 orders of magnitude in contact area, from ~mm^2 to ~$100nm^2$.

4.1 Background

In this chapter an example where the importance of accurate area determination is clearly illustrated will be discussed, namely the effect of pre-stress in substrates on hardness and modulus measurements made by nanoindenters. Studies performed since the 1930's using a range of hardness measurement techniques have indicated a dependence of hardness on applied in-plane uni- and bi-axial strain, and as early as 1952 it was

suggested that such changes could be used to measure residual surface stresses for metals[2-6]. In certain cases, increases in hardness under compressive in-plane strain and decreases in hardness of in-plane tensile strain were observed. To illustrate this trend at the macroscopic scale, Rockwell B hardness data of annealed high-carbon steel from the 1952 Sines and Carlson study[3] has been redrawn in FIG. 4.1(a). The percent change in hardness relative to the unstressed state has been plotted as a function of relative in-plane stress. The applied stress has been normalized by the yield strength for annealed high carbon steel, approximately 350 MPa. This results in a scale varying between -1 and 1, where a value of -1 corresponds to a compressive stress equal to that of the yield strength, 0 is the unstressed state, and 1 corresponds to a tensile stress equal to the yield strength. All hardness values have been normalized to the hardness at the unstressed state. Traditionally this behavior had been attributed to the contribution of stresses from the in-plane strain and the local strain from the indentation to the resolved shear stress. However, like the FS and OP methods described in Chapter 2, the Rockwell hardness test is also empirical in nature. In the test, a known load is applied to the substrate through a steel ball. The depth of the plastic loading is estimated through the machinery of the tester and translated into a hardness number, *i.e. the Rockwell hardness scale*. The accuracy of the test depends on careful calibration using materials of known hardness. In 1996, Tsui, Pharr and Oliver (TPO) [1] pointed out that changes in elastic modulus in pre-stressed substrates relative to the unstressed material appear too large to have physical significance, a result that called into question the interpretation of prior hardness data.

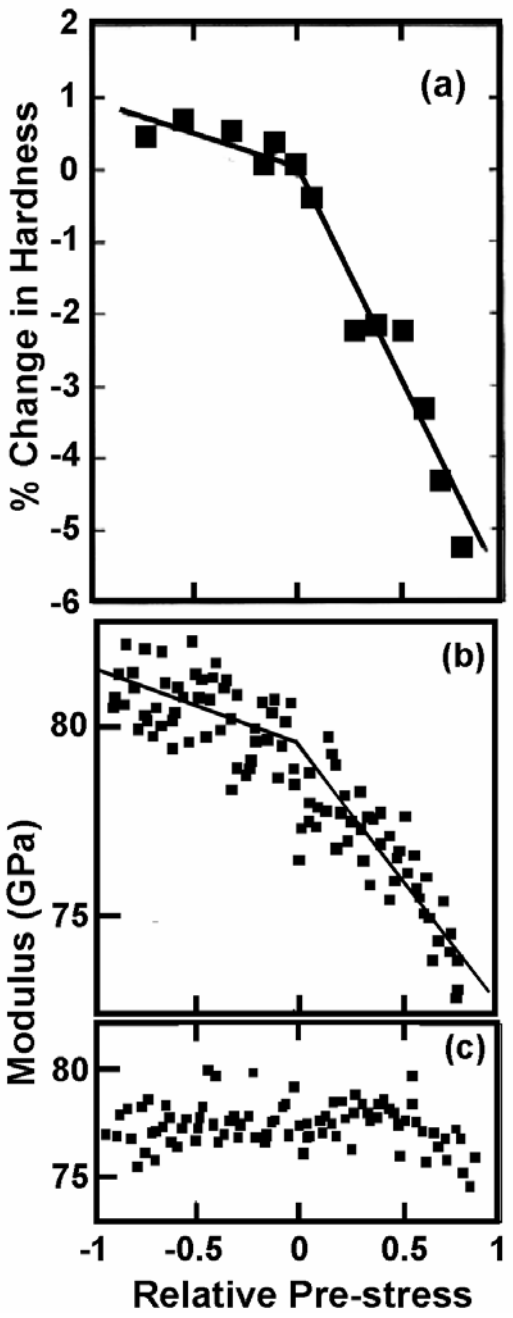

FIGURE 4.1: (a) Sines and Carlson hardness data as a function of relative pre-stress. Percent change in hardness is relative to the hardness at zero pre-stress. Pre-stress is relative to the yield stress reported in reference 12 where negative values denote compression, positive values tension. (b) TPO data for the modulus redrawn from reference 16 as a function of pre-stress calculated using the Oliver-Pharr estimate for the contact area. (c) TPO data for modulus redrawn from reference 1 as a function of relative pre-stress calculated using the optically measured estimate for the contact area. Pre-stress in (b) and (c) relative to the yield stress reported in reference 1.

By indenting a polycrystalline aluminum alloy subjected to varying levels of a uniaxial strain, TPO showed that the slope of the unloading curve portion of the force-displacement curve at maximum load is independent of the strain level. TPO hypothesized that any apparent change in modulus (and hardness) with in-plane strain is primarily due to changes in contact area incorrectly produced by the empirical expressions. Through careful direct optical measurement of the contact impression, they determined that the true contact area was independent of the pre-stress state and thus the modulus is also independent of the pre-stress state. For comparison the modulus data from TPO has been redrawn in FIG 4.1 b and c. The modulus calculated using the empirically estimated contact area is shown in FIG. 4.1b and the modulus corrected using the true contact area is shown in FIG 4.1c. The pre-stress has been normalized by the reported yield strength for the Al alloy used in the TPO experiment (353.1 MPa). The error in the empirical estimates has been shown in experiment and finite element simulations to be due to material pile-up around the indenter[7]. This error is largely minimized in hard materials where pile-up is not present. In further studies using finite element calculations, Chen and Vlassak found that in some cases for soft materials that the contact area may be underestimated using the empirical expressions by as much as 66%[8].

4.2 Simulation approach

As illustrated by this example, the accuracy of the projected contact area approximation or measurement may greatly affect the interpretation of indentation results. Molecular dynamics simulations of spherical indention will be used to compare and contrast the empirical FS and OP area estimates with direct contact area measurement for substrates with a range of pre-existing stresses. The TPO experiments used a Berkovich diamond indenter that left contact impressions on the order $100\mu m^2$. Earlier experimental studies that reported a change in hardness with in-plane stress had much larger contact areas, up to mm^2. Here, the issue of the effect of pre-stress on the modulus and hardness is revisited, but on a much smaller scale (that of about a 100 nm^2 contact area) in single crystal gold, a soft material that shows significant pile-up after a plastic indentation. This scale of contact area is rapidly becoming the realm of features relevant to the electronics industry. The empirically determined areas lead to the same faux change in modulus and hardness as have been found previously. As was shown by the TPO experiments, when direct measurement of contact area is made, changes in modulus are not apparent except at the highest tensile strains. These results, together with prior finite element modeling and experimental studies over a wide range of indentation scales, show that this effect *is remarkably independent of the scale of contact*.

The molecular dynamics code *Paradyn* developed by Plimpton (discussed in Chapter 1) was used to model the indentation of <111> oriented gold surfaces. The indenter-substrate interactions were modeled using the purely repulsive potential form described

in Chapter 3, section 2. The substrate is oriented as shown in FIG. 3.1. The *z* direction is taken to be the normal to a {111} plane. The *x* direction is taken to be along a <110> close-packed direction and *y* is along a <112> direction. The bottom layer of atoms is held rigid in the *z*-direction and the sides are maintained through periodic boundaries in the *x* and *y* directions.

4.3 Results

To study the effect of method of projected area determination on calculation of modulus and hardness, a series of nanoindentation simulations with pre-applied biaxial strains ranging between ±1.5% were conducted, where positive values indicate tension and negative values indicate compression. The substrates consist of 960,000 atoms with unstrained dimensions of approximately 30 nm x 30 nm x 19 nm. Strain was applied uniformly over the entire half-space in the in-plane *x* and *y* directions by multiplying each atomic coordinate by a strain factor $(1+\varepsilon)$ in the x direction and $(1+\sqrt{3}/2\,\varepsilon)$ in the y direction where ε is the applied strain. The factor of $\sqrt{3}/2$ ensures that the symmetry of the (111) plane is maintained. To maintain strain, the periodic boundary lengths in the x and y directions were also multiplied by their respective strain factors. The energy of the substrate was then minimized via a conjugate gradient step to achieve the correct contraction or expansion in the z direction. After minimization, the substrate was heated to 300K and allowed to equilibrate using the generalized Langevin thermostat. Each substrate was then indented with a 100 Å radius indenter to a maximum load of approximately 4700 nN, which resulted in penetration depths between 16 Å for a strain of

-1.5% and 19 Å for 1.5% a strain. Permanent deformation was present upon unloading indicating the presence of plastic damage even though no discontinuities or pop-in events were observed in the force-displacement curves, see FIG. 4.2. Interestingly, the true contact area in our simulations (as determined by the IP method) changes continuously with depth throughout the indentation cycle as illustrated in FIG 4.3a. The algorithm for the inscribed polygon calculation is presented in Appendix A. The contact impression is fairly circular and its perimeter only marginally reflects the underlying crystal symmetry as illustrated by the contact impression shown in FIG. 4.3b. This behavior is significantly different from the discrete steps in the contact area as a function of depth and clear reflection of crystal symmetry observed for simulations where a conjugate gradient minimization method was employed. These differences are attributed to the random thermal motion of atoms present in these simulations that are not present when conjugate gradient methods are used.

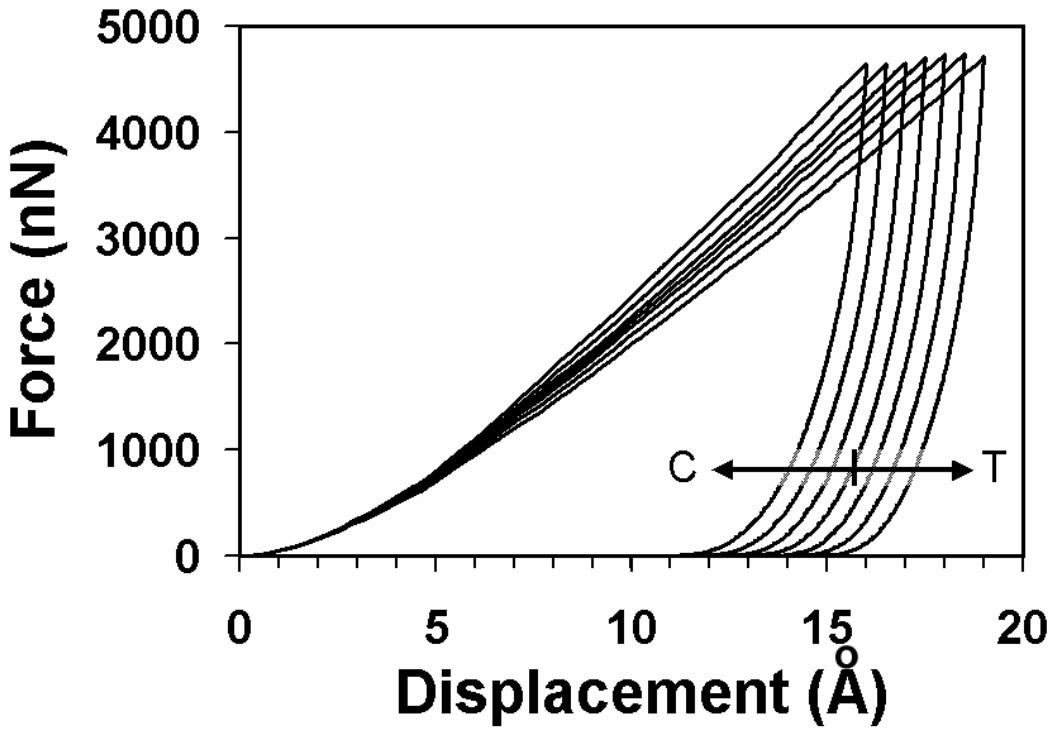

FIGURE 4.2: Force-displacement curves for substrates with different levels of an applied pre-stress. Each substrate was loaded to approximately 4700 nN. C denotes loading curves under compressive pre-strain up to -1.5%. T denotes substrates under tensile pre-strain up to 1.5%.

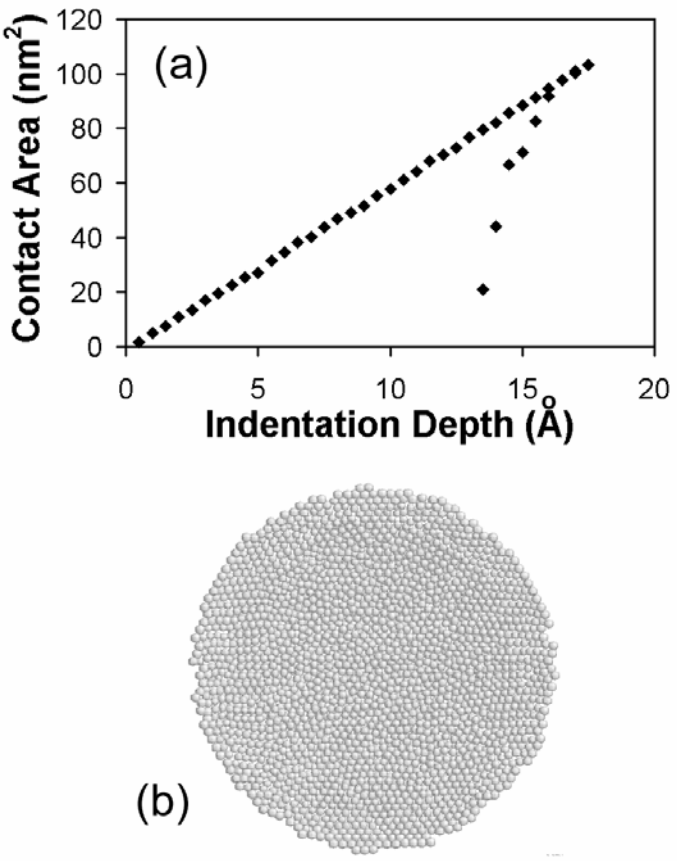

FIGURE 4.3: (a) True contact area as measured by the inscribed polygon method as a function of indenter displacement for loading and unloading of the unstressed sample and (b) the disk atoms in contact with the indenter at maximum load for the unstressed sample. The diameter of the disk is roughly 120 Å.

The analysis is begun by determining the projected contact area for each indentation. As suggested above, the true contact area may be determined *in situ* using the IP method since the atomic coordinates of the perimeter of contact may be determined at any time step during the simulation. The projected contact area as determined using the FS approximation may be determined directly from the unloading curve. Determining the projected contact area using the OP method first requires that the unloading stiffness at

the peak load be determined. The unloading stiffness was calculated by a linear least squares fit to the first ten data points of the unloading curve. Shown in FIG. 4.4 is the unloading stiffness plotted as a function of relative pre-stress.

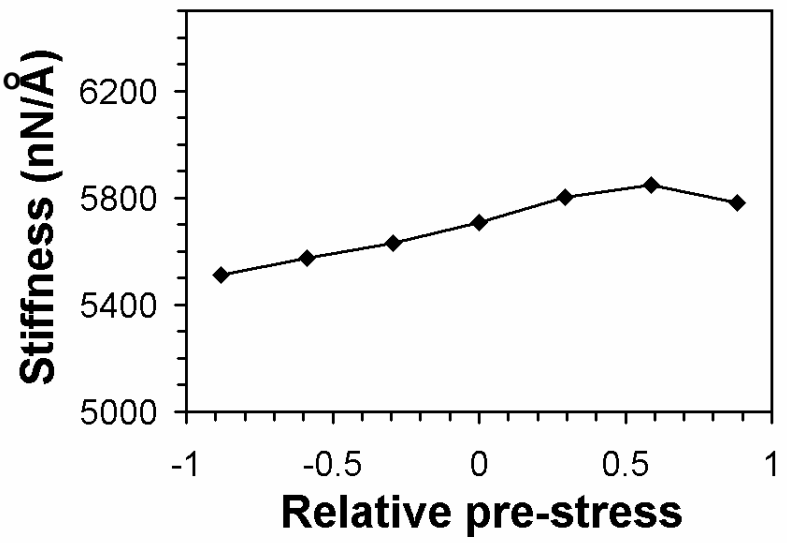

FIGURE 4.4: The unloading stiffness as a plotted as a function of the relative pre-stress. (1 nN/Å = 10 N/m)

Contrary to the experiments of TPO, the unloading stiffness is not independent of the pre-stress level. In FIG. 4.4 and subsequent figures, the pre-stress was calculated from the applied biaxial pre-strain using Hooke's law. For comparison to the experimental data of Sines and Carlson and TPO data in FIG. 4.1, each pre-stress level was then normalized by the yield strength. Again, this gives a scale varying between -1 and 1 where a value of -1 corresponds to a compressive stress equal to that of the yield strength, 0 is the unstressed state, and 1 corresponds to tensile stress equal yield strength. Because the material is

single crystal and is initially defect and dislocation free we have assumed that the yield stress is equal to the theoretical yield strength of gold. This value was determined using the Frenkel approximation using the expression $\tau_{th} = Gb/a2\pi$, where *G* is the shear modulus, *b* is the distance between atoms in the slip direction and *a* is the distance between slip planes. The projected contact areas, as determined using all three methods, have been plotted as a function of the relative pre-stress in FIG 4.5a. The FS areas are indicated by open diamonds, the OP areas are indicated by open triangles, while the true IP areas are represented by filled squares. The percent error of the FS (open diamonds) and OP (open triangles) estimated areas relative to the true (IP) contact area is shown in FIG 4.5b. The error is not consistent across the range of the pre-stress and the amount of error tends to be higher in compression than in tension. This will cause errors in not only the relative values of the hardness and modulus but also the dependence in the hardness and modulus with the applied pre-stress. At the highest level of compressive pre-stress the FS method underestimates the contact area by as much as 27%. The OP method is somewhat better with a maximum underestimation of area in compression of 9%. The lowest values of error appear in tension and are 16% and 5% for the FS and OP method respectively. It should also be noted that the true contact area as calculated by the IP method is not independent of the pre-stress level, contrary to the results of the TPO experiments.

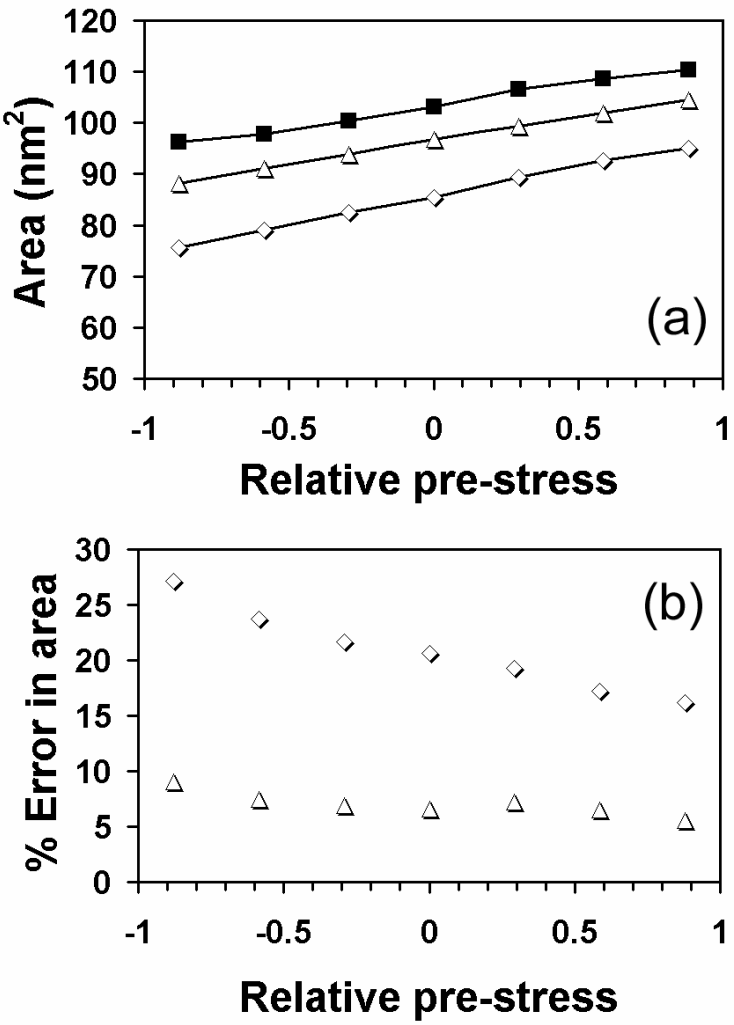

FIGURE 4.5: (a) The projected contact area as a function of the relative pre-stress for true area (filled squares), OP area (open triangles), and FS area (open diamonds) and b) the percent error in the area estimation with respect to the true contact area for the OP method (open triangles), and FS method (open diamonds) as a function of the relative pre-stress.

To illustrate the extent of the errors caused by the empirical formulas, the mean pressure and reduced modulus as calculated from Eqs. 2.1 and 2.2 using the areas from all three methods have been plotted in FIGS. 4.6a and 4.7a. The percent change in mean pressure and modulus relative to the zero pre-stress state has been plotted in FIGS 4.6b and 4.7b.

In both FIGS. 4.6 and 4.7, the open diamonds represent the mean pressure or reduced modulus determined using the FS model, open triangles represent the mean pressure or modulus determined using the OP method, and the filled squares represent the mean pressure or modulus determined using the true area from the IP method. As illustrated in FIG 4.6a, the FS method causes a large over estimation in the mean pressure with the largest overestimation in compression. The OP method also overestimates the mean pressure but to a much smaller extent. In these simulations, the mean pressure is dependent on the pre-stress even when the true contact area is used since the true contact area is not independent of the pre-stress level, a result different from the TPO findings. As illustrated by FIG 4.6b, the OP method appears to model this trend very well except at the highest compressive pre-stress level, while the FS model tends to exaggerate the trend to a large degree. The same general results are observed in the modulus calculations shown in FIG 4.7a. Again the FS model greatly overestimates the modulus, while the OP method provides a better but still high estimate. Despite the fact that a dependence of both the true contact area and the unloading stiffness on the pre-stress level is observed, the ratio of the stiffness to the square root of the true contact area appears to be independent of the pre-stress level. When the true contact area is used in the modulus calculation little or no change relative to the unstressed state is observed except at the highest tensile pre-stress level, a trend that was also observed by Tsui, Pharr, and Oliver (compare to FIG 4.1c). The OP method does a good job estimating the dependence (or lack of) of the modulus on the pre-stress level except at the highest compressive pre-stress level, as seen in FIG 4.7b, while the FS model suggests a false dependence of modulus on the pre-stress level similar to the data shown in FIGS 4.1a and 4.1b.

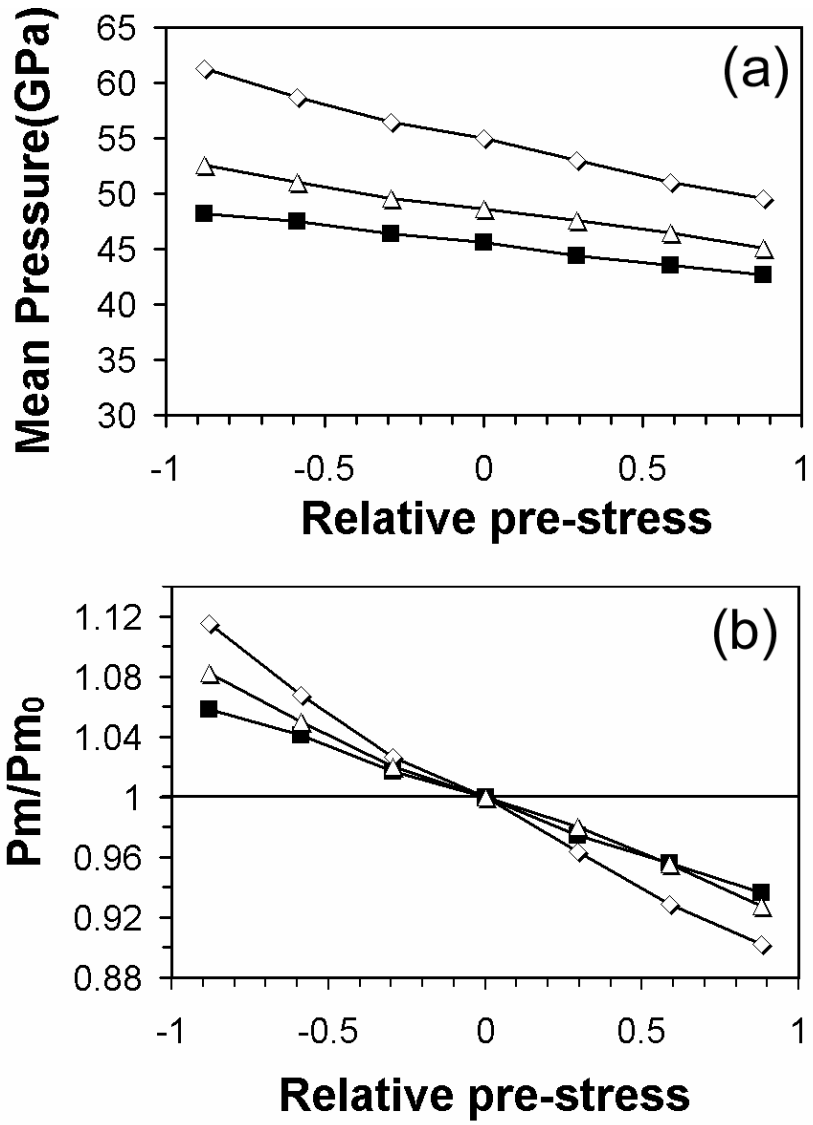

FIGURE 4.6(a) Mean pressure as a function of relative pre-stress as calculated using the true area (filled squares), OP method (open triangles), and FS method (open diamonds) and (b) the relative mean pressure with respect to the mean pressure at zero pre-stress for the true area (filled squares), OP method (open triangles), and FS method (open diamonds).

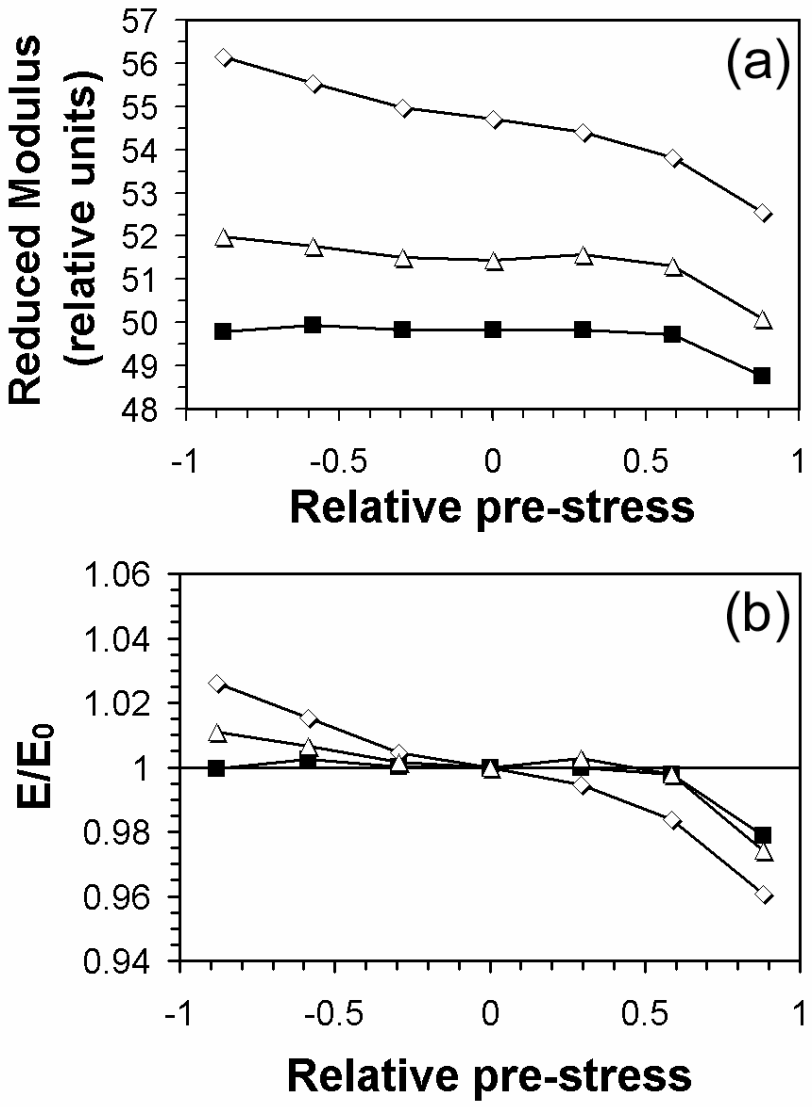

FIGURE 4.7(a) Reduced Modulus as a function of relative pre-stress as calculated using the true area (filled squares), OP method (open triangles), and FS method (open diamonds) and (b) the relative reduced modulus with respect to the reduced modulus at zero pre-stress for the true area (filled squares), OP method (open triangles), and FS method (open diamonds).

4.4 Plastic deformation

Plastic damage was investigated using the slip-vector parameter. A detailed description of the slip vector calculation is given in Appendix B. The results of these calculations

are shown for compressive, tensile, and no biaxial pre-stress in FIG 4.8. Clearly different slip systems are active for different biaxial pre-stresses. Compressive pre-stress shows the most significant deviation in slip behavior. In this case dislocation loops radiate out and away from the indenter. In the tensile and no stress cases the damage tends to be localized beneath the tip. The radial distribution of 'slipped' atoms with respect tip is show in FIG 4.9. A deeper understanding of these differences in plastic behavior may help understand the trail-off in the elastic modulus in samples under tension observed in both experiment (FIG 4.1c) and the simulated data (Fig 4.7).

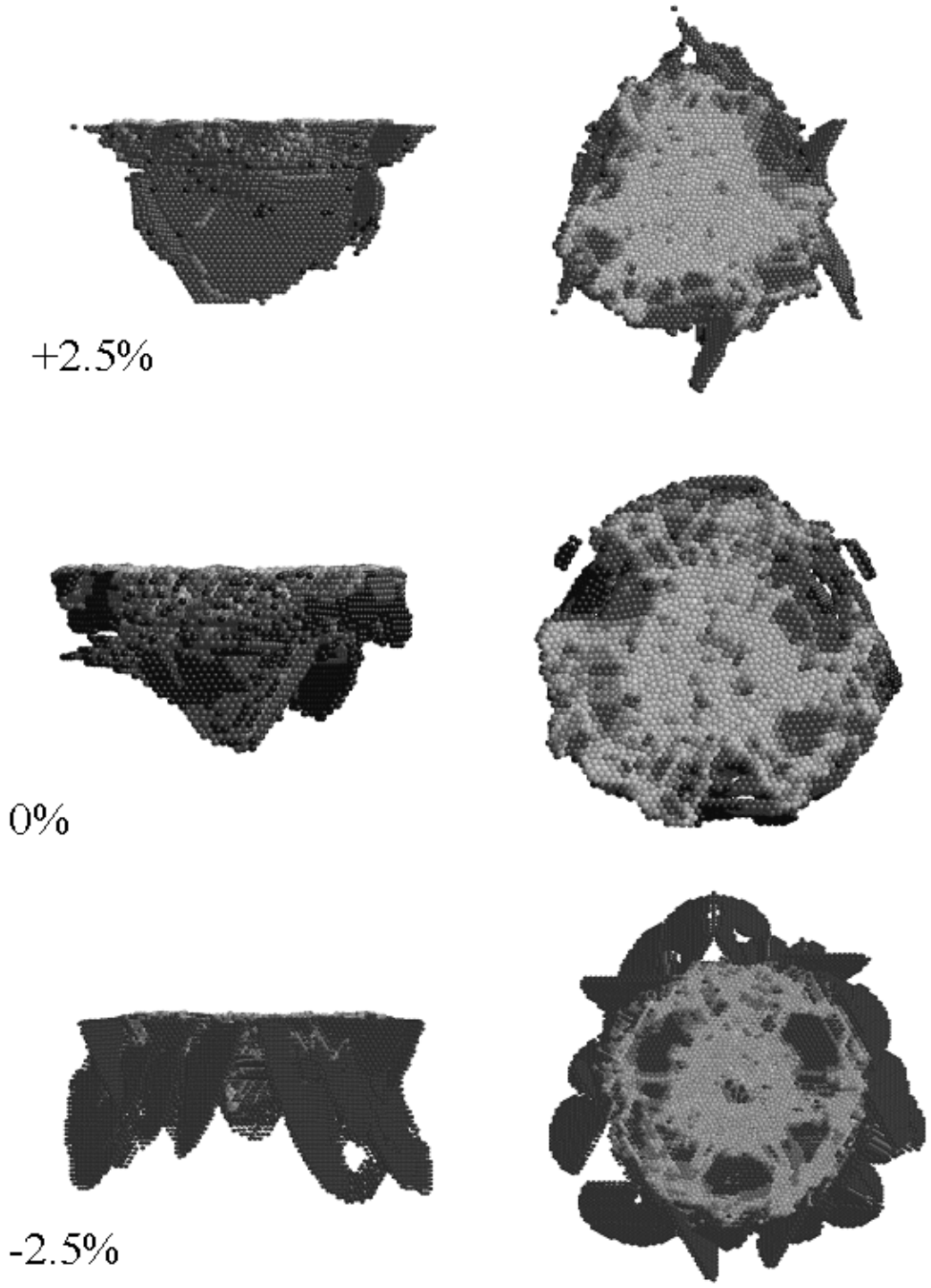

FIGURE 4.8: Damage due to nanoindentation calculated using the slip vector calculation with a cut of value of 0.5 Å for 2.5%, 0% and -2.5% biaxial strains, Side views left, top views right.

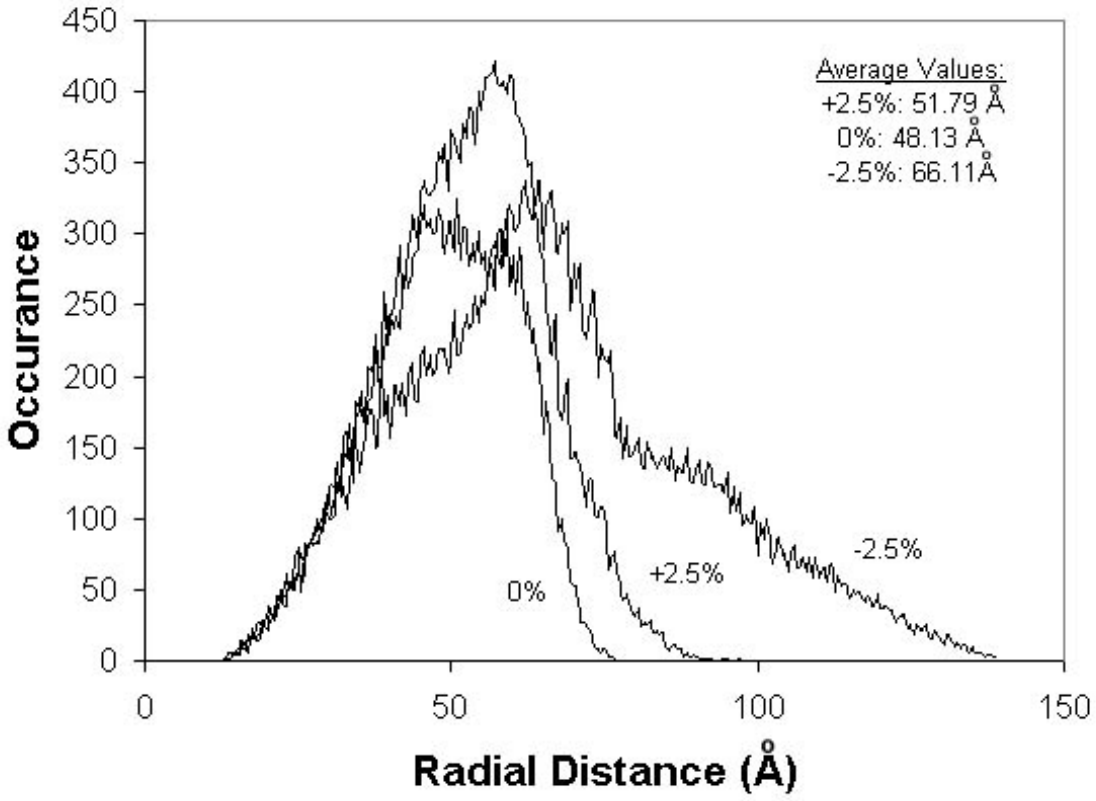

FIGURE 4.9: Damage profile due to nanoindentation based on slip-vector cut-off of 0.5 Å.

4.5 Discussion

Through the use of molecular dynamics simulations, the importance of accuracy in the calculation or measurement of the projected contact area on the interpretation of nanoidentation results has been illustrated. Based on these results, it appears that although the OP method underestimates the projected contact area and thus overestimates the mean pressure and modulus, it does a fairly good job for the system modeled at predicting the dependence of pre-stress on the mean pressure and modulus except at very

high levels of the pre-stress. However, it should be noted that the same method failed to predict the correct results in the experiments of Tsui, Pharr, and Oliver. It has been shown that simpler empirical area estimations fail miserably to predict even the correct dependencies. By way of comparison of these simulations to experiments in published literature show that determining the correct value of contact area is important to the correct interpretation of indentation results across a wide range of length scales: from square nanometers to square millimeters. A certain wariness of empirical estimates for contact areas and properties derived from them is advised when interpreting the results of new experiments or those published in the past. However, when the true contact area is used values for mean pressure and modulus may be relied upon.

4.6 References

1. 1. T.Y. Tsui, W.C. Oliver and G.M. Pharr, *J. Mater. Res.* 11, 1996,752.

2. S. Kokubo, *Science Reports of the Tohoku Imperial University*. 21, 1932,256.

3. G. Sines and R. Carlson, *ASTM Bulletin.* 180, 1952, 35.

4. G.U. Oppel, *Exp. Mech.* 21, 1964, 135.

5. T.R. Simes, S.G. Mellor and D.A. Hills, *J. Strain Analysis*. 19, 1984,135.

6. W.R. LaFontaine, C.A. Paszkiet M.A. Korhonen, and Che-Yu Li, *J. Mater. Res.* 6, 1991, 2084.

7. A. Bolshakov, W.C. Oliver and G.M. Pharr, *J. Mater. Res.* 11, 1996,760.

8. X. Chen and J.J. Vlassak, *J. Mater. Res.* 16, 2001, 2974.

5. THE INFLUENCE OF PRE-EXISTING STRESS ON THE INTERPRETATION OF NANOINDENTATION DATA – ELASTIC INDENTATION

It is well known that the elastic constants of a bulk material do in fact change with strain due to anharmonicity in the interatomic potentials, and a number of experimental and theoretical studies of this phenomena have been conducted in the past for single crystal whiskers, grain boundaries and twist boundaries, etc [1-4]. that illustrate this behavior. Yet, this stress dependence has not been observed or measured in nanoindentation experiments (in a real way). The question addressed in this chapter is "Is it possible to detect these changes using indentation techniques?"

5.1 Introduction and background

Although not explicitly discussed, data from several recently published theoretical studies concerning the mechanisms of the onset of plastic deformation during nanoindentation, and the relationship of these details to surface and near-surface structures, indicate subtle differences in load-displacement curves below the yield point that may indicate local changes in elastic behavior of the material. Shenderova *et al*. explored the issue of whether very shallow elastic nanoindentation can be used to nondestructively probe surface stress distributions associated with surface structures such as a trench and a dislocation intersecting a surface [5]. The simulations, which carried out indentation to a constant depth, showed maximum loads that reflected the in-plane stresses at the point of contact. In related work, Zimmerman *et al.* used simulations employing embedded-atom method potentials to model

indentation of a single-crystal gold substrate both near and far from a surface step [6]. These simulations show that the onset of plastic deformation (which occurs via nucleation of dislocations) is strongly influenced by the distance of indentation from the step, and whether the indentation is on the plane above or below the step. Careful examination of their force-displacement curves indicate that the initial slope before the onset of plastic deformation noted by the sudden discontinuity in the force-displacement curve appears to reflect the different surface stresses above and below a surface step. More recently Lilleodden *et al.* used a similar atomic-level simulation methodology to show that grain boundaries in the vicinity of a nanoindentation point can produce dislocations that influence the plastic behavior of the substrate [7]. Again, the initial slope of the load-displacement curve depends on the proximity of the indentation to the grain boundary.

Based on these observations, we conducted a series of molecular dynamics simulations of shallow, purely elastic nanoindentations in biaxially strained gold substrates and have investigated the potential of such indentations to predict real changes in elastic modulus with biaxial strain. The simulations show changes in loading curves do reflect changes in surface stress as long as the plastic limit is not reached. The dependence of the indentation modulus determined from these simulated nanoindentation experiments on the applied biaxial strain agrees qualitatively with the dependence derived from an analysis of the second- and third-order elastic constants in bulk single crystal (i.e. true change in modulus with applied strain).

5.2 Method

The molecular dynamics code *Paradyn* developed by Plimpton[8] was used to model the indentation of [001] and [111] oriented gold surfaces. A series of nanoindentation simulations with pre-applied biaxial strains ranging between ±1.5% were conducted. Here positive values of strain indicate tension and negative values indicate compression. The rigid indenter described in Chapter 3 was used to make the indentations. Each substrate consists of roughly 300,000 atoms with unstrained dimensions of approximately 30 nm x 30 nm x 6 nm. Strain was applied to the [001] oriented substrate uniformly over the entire half-space in the in-plane *x* and *y* directions using the strain factor $(1+\varepsilon)$. In the [111] oriented substrate, strain was applied by multiplying a strain factor $(1+\varepsilon)$ in the *x* direction and $(1+\sqrt{3}/2\,\varepsilon)$ in the *y* direction where ε is the applied strain. The factor of $\sqrt{3}/2$ ensures that the symmetry of the (111) plane is maintained. To maintain strain, the periodic boundary lengths in the x and y directions were also multiplied by their respective strain factors. The energy of the substrate was then minimized via a conjugate gradient step to achieve the correct contraction or expansion in the *z* direction. After minimization, the substrate was heated to 300K and allowed to equilibrate. Each substrate was then indented with a 4 nm radius indenter to a depth of 2.5Å at a constant rate of 0.5 Å/ps. The force-displacement curves generated from these simulations were used to calculate the indentation modulus. These are compared to the indentation modulus calculated from the bulk elastic properties of gold.

5.3 Calculation of elastic constants in bulk material

The second-order elastic constants (three independent constants for cubic materials) can generally be obtained by applying a strain to the lattice and calculating the second derivative of the energy using a molecular statics calculation [3]. The bulk modulus is defined as

$$B = \frac{a_0^2}{9V}\frac{\partial^2 E}{\partial a^2} \qquad \text{Eq. 5.1}$$

where a_0 is the equilibrium lattice constant, V is the atomic volume, and $\frac{\partial^2 E}{\partial a^2}$ is the second derivative of energy E with respect the lattice parameter a. To determine the bulk modulus, the lattice parameter a is varied uniformly in the x, y, and z to give a uniform volume expansion or contraction. Similarly the shear constant C' may be determined using the expression

$$C' = \frac{a_0^2}{4V}\frac{\partial^2 E}{\partial a^2} \qquad \text{Eq. 5.2}$$

Here the lattice is subjected to dilation in one direction and contraction along the other, while maintaining a constant volume. Strain is applied such that constant volume is maintained $\varepsilon_x = \varepsilon$, $\varepsilon_y = -\varepsilon$, $\varepsilon_z = 0$. Bulk and shear modulii are defined in terms of the elastic constants C_{11} and C_{12} as

$$\begin{aligned} B &= (C_{11} + 2C_{12})/3 \\ C' &= (C_{11} - C_{12})/2 \end{aligned} \qquad \text{Eqs. 5.3}$$

By solving Eqs. 5.3 simultaneously it is possible to calculate C_{11} and C_{12} in terms of B and C'

$$C_{12} = (3B - 2C')/3$$
$$C_{11} = 2C' + (3B - 2C')/3 \qquad \text{Eqs. 5.4}$$

The third independent elastic constant C_{44} is defined as follows

$$C_{44} = \frac{a_0^2}{4V}\frac{\partial^2 E}{\partial a^2} \qquad \text{Eq. 5.5}$$

where this case *a* is a lattice shear strain. In the PARADYN code, only strains that conform to the repeating cubic boundary conditions can be applied – shears will not work. For a [001], oriented FCC lattice (defined as z along the [001]) the solution is simple. A Bain strain is applied to a BCC [001] oriented cell so that the BCC unit cell is transformed to a FCC [001] unit cell rotated 45 degrees about the [001] axis so that the [110] direction is along the *x* and [-110] is along the *y*. Strains are applied to this lattice in the same way as for the shear constant C' with lattice dilation in one direction and contraction in another, while the third is held constant so that $\varepsilon_x = \varepsilon$, $\varepsilon_y = -\varepsilon$, $\varepsilon_z = 0$. This results in shear strains on the [100] and [010] directions.

5.4 Calculation of indentation modulus from bulk elastic constants

The anisotropic Hertzian contact problem defines the indentation modulus E_R as $E_r = \frac{S}{2}\sqrt{\frac{\pi}{A}}$ as shown before in Chapter 2. The indentation modulus generally depends on the shape of the indenter, except in certain cases of crystal symmetry. Using the formalism of Barnett and

Lothe[8], Vlassak and Nix[9] derived simple expressions for the indentation modulus for circular flat punches. The same approach was extended to conical and spherical indenters used by Swadener and Pharr[11]. They have shown that for isotropic materials and anisotropic-axisymmetric geometries, the indentation modulus reduces to the plane-strain elastic modulus $E_R = \frac{E}{1-\nu^2}$ independent of the indenter shape as indicated before in Eq. 2.3. In anisotropic-axisymmetric materials, such as cubic materials oriented along crystallographic directions with high symmetry such as the <001> and <111> directions, the indentation modulus is then given as

$$E_{R(hkl)} = \frac{E_{(hkl)}}{1-\nu_{(hkl)}^{\ 2}} \qquad \text{Eq. 5.6}$$

where *hkl* are the crystallographic indices normal to the surface that can be determined from the bulk elastic constants C_{11}, C_{12}, and C_{44}[11]. Anisotropic materials with non-axisymmetric orientations require much more complex solutions involving Green's functions and Fourier solutions to large integral equations. The expressions for $E_{(hkl)}$ and $\nu_{(hkl)}$ for <001> and <111> crystallographic orientations are give below[2]:

$$E_{001} = C_{11} - 2C_{12}\nu_{001} \qquad \text{Eq. 5.7}$$

with

$$\nu_{001} = \frac{C_{12}}{C_{11} - C_{12}} \qquad \text{Eq. 5.8}$$

$$E_{111} = \frac{1}{3}\left[\left(C_{11} + 2C_{12} + 4C_{44}\right) - \left(2C_{11} - 4C_{12} - 4C_{44}\right)\nu_{111}\right] \qquad \text{Eq. 5.9}$$

with

$$\nu_{111} = \frac{C_{11} + 2C_{12} + 2C_{44}}{2\left(C_{11} + 2C_{12}\right) + 2C_{44}} \qquad \text{Eq. 5.10}$$

5.5 Results

The force-displacement curves for a series of shallow nanoindentation simulations using the rigid indenter are plotted in FIGS. 5.1 and 5.2. Each figure shows different curves for substrates with varying levels of applied biaxial in-plain strain. The changes in the slope of the force-displacement curves suggest a dependence on the level of biaxial strain in each substrate. Data from each of these curves was used to determine the effective indentation modulus using the Hertzian solution given by Eq. 2.2 and the power law solution given in Eq. 3.4.

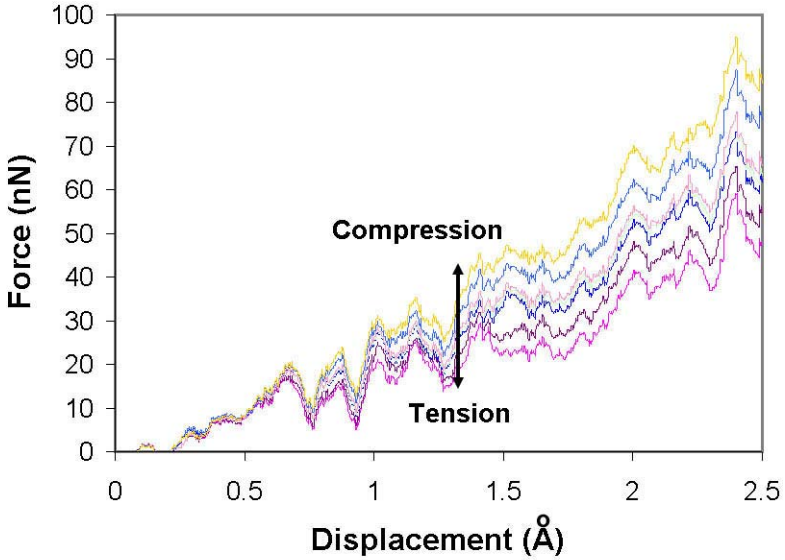

FIGURE 5.1: Force-displacement curves for a [001] oriented substrate indented with a 4 nm rigid indenter with an indentation rate of 0.5 Å/ps.

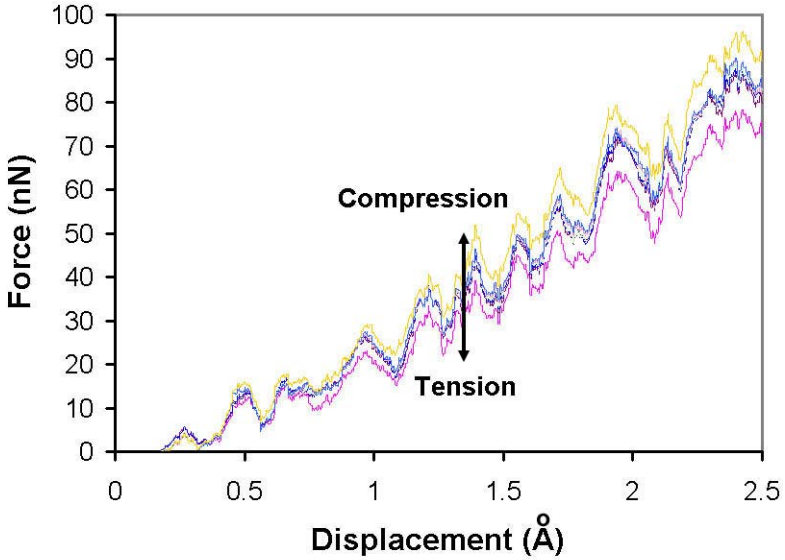

FIGURE 5.2: Force-displacement curves for a [111] oriented substrate indented with a 4 nm rigid indenter with an indentation rate of 0.5 Å/ps.

It is assumed that the indentation of the substrate is in the linear elastic regime, the unloading curve is the same as the loading curve, and that the unloading stiffness is equal to the derivative of the loading curve. In practice, there is a small hysteresis in the curve and thus not truly linearly elastic. Given this assumption, the value of stiffness S in Eq. 2.2 is determined by taking the derivative of a power-law fit $P = kh^m$ of the force-displacement data, $S = \frac{dP}{dh} = mkh^{m-1}$. The results of these calculations are shown in FIGS. 5.3 and 5.4.

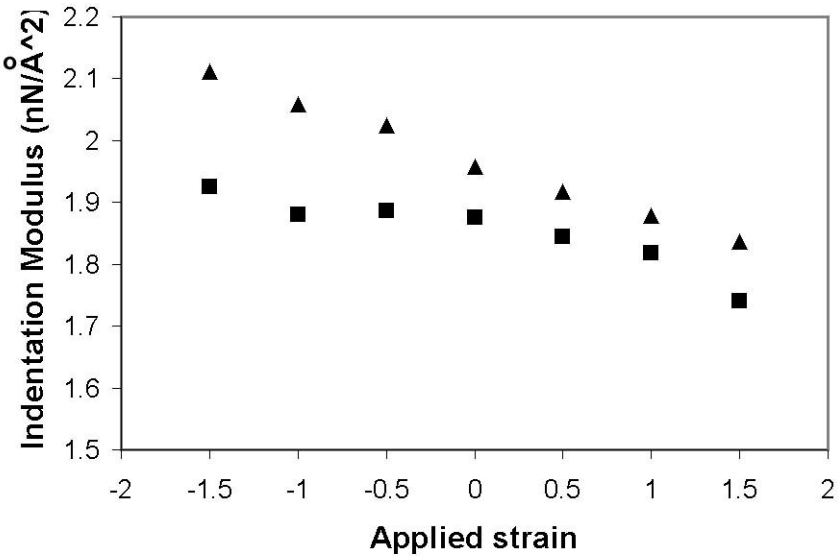

FIGURE 5.3: Indentation modulus for a [001] oriented substrate calculated by Eq. 2.2 (squares), and Eq. 3.4 (triangles). (1 nN/Å^2 = 100 GPa)

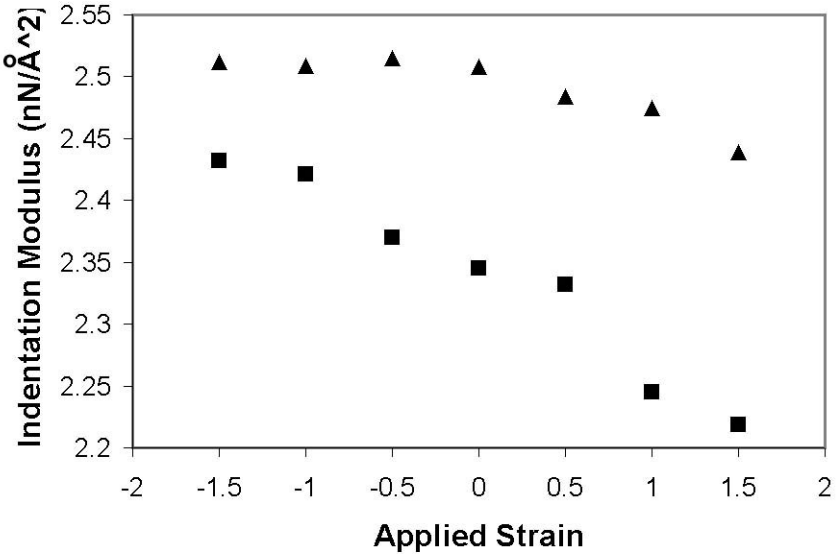

FIGURE 5.4: Indentation modulus for a [111] oriented substrate calculated by Eq. 2.2 (squares), and Eq. 3.4 (triangles). (1 nN/Å^2 = 100 GPa)

Although the power law calculation using Eq. 3.4 and the Hertz solution in Eq. 2.2 are not in quantitative agreement with each other, FIGS. 5.3 and 5.4 show a clear dependence of the modulus on the applied strain.

5.6 Determination of indentation modulus as a function of biaxial in-plane strain using bulk elastic constants

Using Eqs. 5.1, 5.2, and 5.5, the three independent elastic constants C_{11}, C_{12}, and C_{44} were determined for [001] and [111] oriented bulk material as a function of biaxial strains applied in the (001) and (111) planes respectively. This is essentially a calculation of the third-order elastic constants with respect to these directions. These constants were then substituted into equations 5.7 and 5.8 to calculate E and ν which were in turn used to determine the indentation modulus in using Eq. 5.6. This calculation proceeds in a straight forward manner

for the [001] oriented bulk crystal. A uniform biaxial strain is applied to the bulk crystal and Eqs. 5.1, 5.2 and 5.5 are evaluated. The atomic volume term V in these equations is modified from $V = \frac{a_0^3}{4}$ to

$$V = \frac{a_0^3}{4}(1+\varepsilon)(1+\varepsilon) \qquad \text{Eq. 5.11}$$

where ε is the applied biaxial strain. This accounts for the change in the atomic volume due to the applied biaxial strain. The results of these calculations are shown in FIG. 5.5. As expected the values of C_{11}, C_{12}, and C_{44} for the unstrained bulk crystal match the values reported for the EAM potential given in Table 3.1.

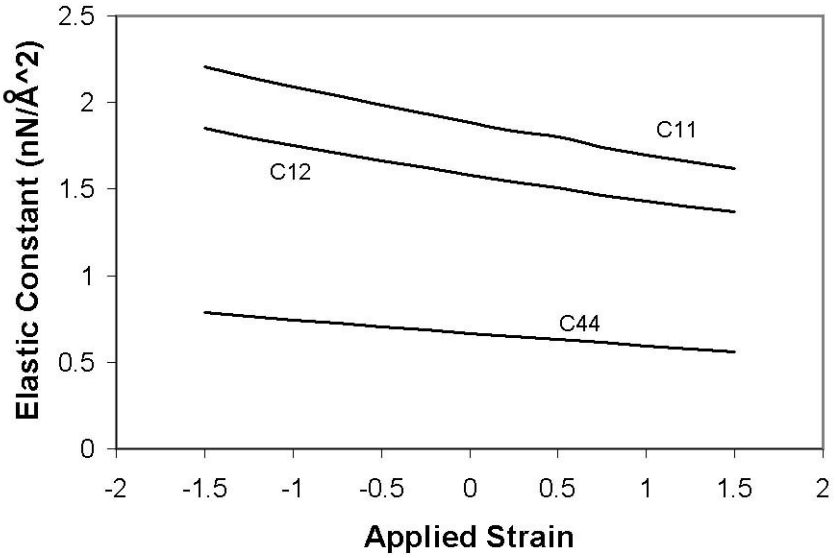

FIGURE 5.5: Elastic constants as a function of applied strain for [001] oriented bulk. Biaxial strain applied in the (001) plane. (1 nN/Å^2 = 100 GPa)

Determination of the dependence of the indentation modulus of a [111] oriented substrate on biaxial strains applied to the (111) plane is more difficult. At first glance it may seem that substitution of the strain-dependent elastic constants determined for the [001] oriented bulk crystal into Eqs. 5.9 and 5.10 is the logical solution. However, this would reproduce the wrong strain-dependence, namely that of the [111] indentation modulus on strain in the (001) plane, which is physically meaningless. Instead we calculate the elastic constants $C_{11(111)}$, $C_{12(111)}$, and $C_{44(111)}$. These are not the true elastic constants but the elastic constants as determined for the [111] direction. Eqs. 5.1 and 5.2 are evaluated as before, except with the bulk crystal oriented with the [111] direction along the *z* axis. In this case the atomic volume was adjusted to

$$V = \frac{a_0^3}{4}(1+\varepsilon)(1+\sqrt{3}/2\varepsilon) \qquad \text{Eq. 5.12}$$

The factor $\sqrt{3}/2$ is required to maintain the symmetry of the (111) plane.

The determination of $C_{44(111)}$ is more difficult. To rotate the FCC [111] oriented lattice (z along [111]) by 45 degrees as is required to evaluate Eq. 5.5 is non-trivial. The reorientation does not accommodate convenient periodic boundaries. A large FCC [111] oriented lattice with [1-10] along *x*, [-1-12] along *y* was generated and rotated by 45 degrees around the [111] direction and a suitable minimum lattice repeat unit was selected. The lattice was then relaxed using conjugate gradient minimization, in a constant pressure ensemble. The periodic boundaries were changed so that the zero pressure was maintained. The symmetry in the (111) plane, as measured by the angles between <110> directions in the (111) plane was maintained with in 0.1%. A single layer of the repeat cell is shown in FIG 5.6. The elastic constants determined through this set of calculations are shown in FIG. 5.7.

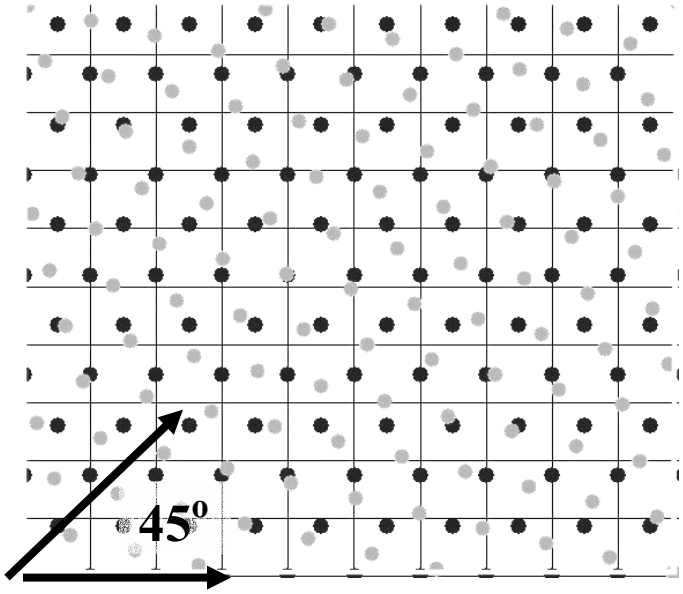

FIGURE 5.6: Schematic diagram of a single (111) plane in the un-rotated (black dots) lattice and rotated (gray dots) lattice.

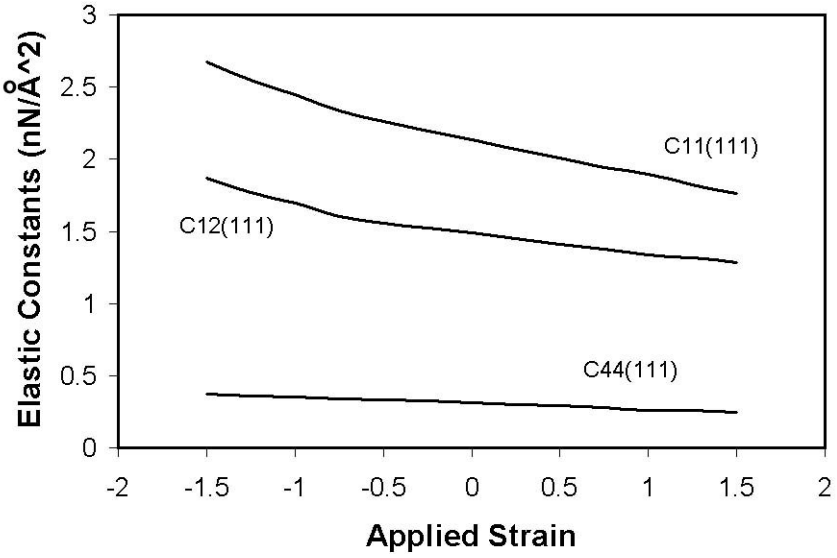

FIGURE 5.7: Elastic constants as a function of applied strain for [111] oriented bulk. Biaxial strain applied in the (111) plane. (1 nN/Å^2 = 100 GPa)

The bulk elastic constants were then used to calculate the indentation modulus using Eqs. 5.6, 5.7 and 5.8. The results of these calculations are given in FIG. 5.8.

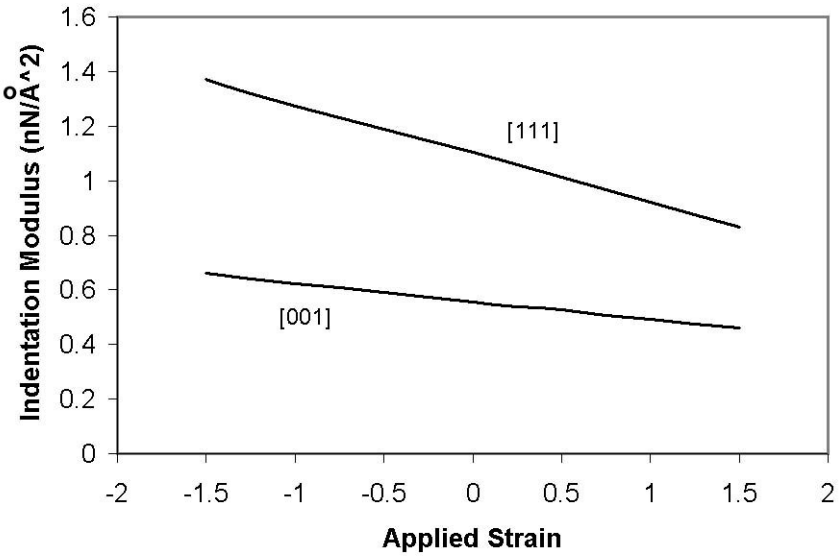

FIGURE 5.8: Indentation modulus as a function of applied biaxial strain calculated from bulk elastic constants for orientations along [111] with strain applied in the (111) plane and oriented along [001] with strain applied in the (001) plane. (1 nN/Å^2 = 100 GPa)

5.7 Comparison of bulk indentation modulus to simulated indentation modulus

Comparison of indentation modulus calculated from the bulk elastic constants shown in FIG. 5.8 to the indentation modulus calculated from the simulated nanoindentation experiments shown in 5.3 and 5.4 suggest that the nanoindentation simulations overestimate the true indentation modulus. The bulk elastic constants are determined in a static energy calculation. The use of these constants in the calculation of the indentation modulus should in principle only be valid in the case of static loading. This is clearly not the case in the simulations of

nanoindentations presented here. A series of simulated nanoindentation experiments with indentation rates varying between 2 and 0.01 Å/ps was conducted on a [001] unstrained substrate. Even slower indentation rates (< 0.01 Å/ps) become very computationally expensive. The indentation modulus from these simulations has been plotted as a function of indentation rate, shown in FIG 5.9. At slower rates the indentation modulus appears to converge towards the static value determined from the bulk elastic constants supporting this hypothesis.

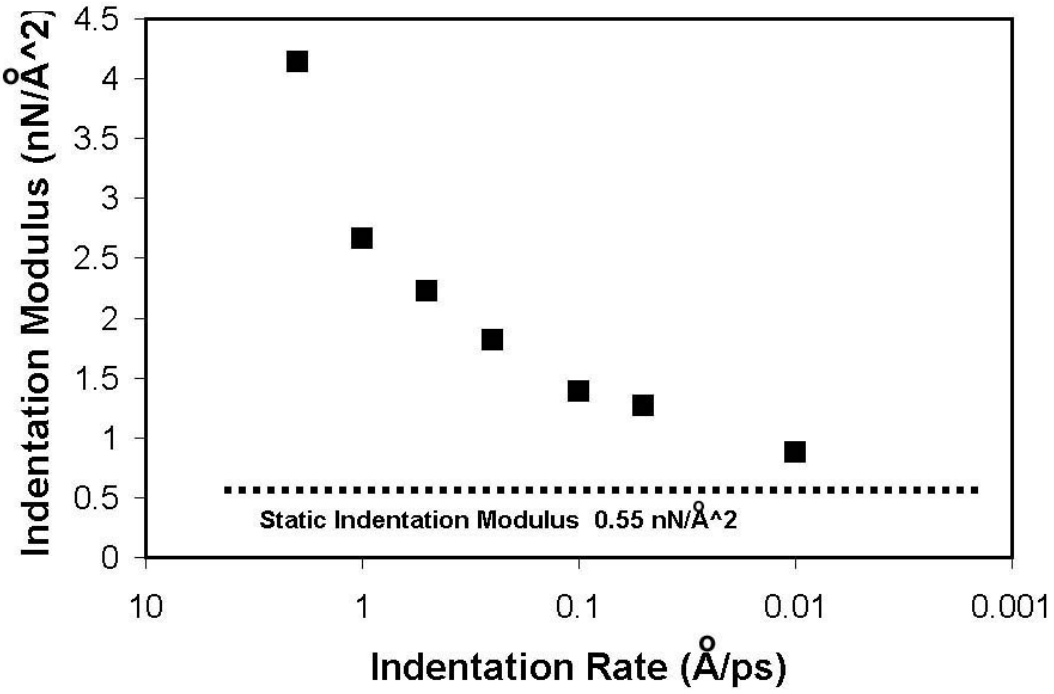

FIGURE 5.9: Indentation modulus from simulated indentation of a [001] oriented substrate as a function of the indentation rate. As the rate decreases the indentation modulus appears to approach the static value for the indentation modulus (shown as by the dotted line) determined using the bulk elastic constants. (1 nN/Å^2 = 100 GPa)

The assumption has been made that the dependence of indentation modulus on indentation rate does not change with applied strain. Using this assumption, the indentation modulii calculated from the simulated nanoindentation experiments normalized to the same scale as the indentation modulus calculated from the bulk elastic constants have been plotted as a function of the applied biaxial strain as shown in FIGS 5.10 and 5.11. The indentation modulus of the unstrained state was used as the normalizing factor for each calculation method. In FIG. 5.12, the indentation modulus of the [001] and [111] substrates are plotted on the same graph. This plot is in good qualitative agreement with FIG. 5.8.

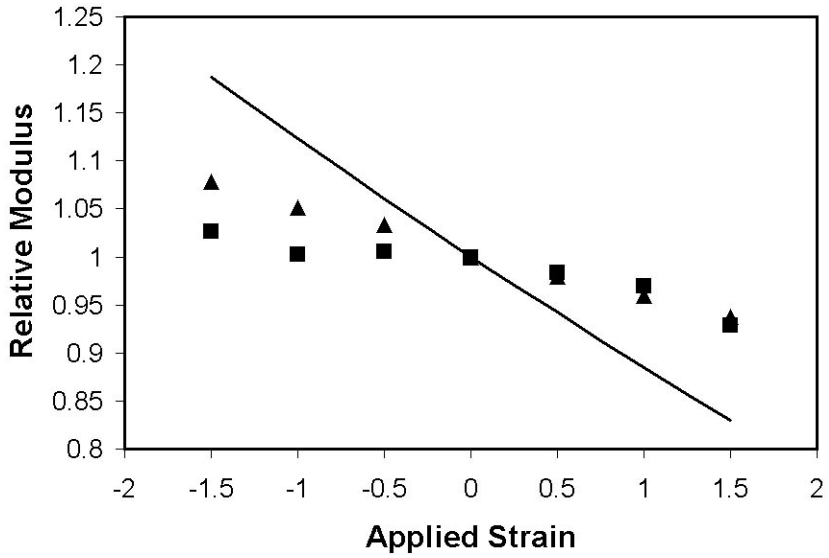

FIGURE 5.10: The relative indentation modulus for a [111] oriented substrate as a function of applied strain for the power law fit to simulated indentation data (triangles), Hertzian calculation using simulated indentation data (squares) and the response expected from the calculation using the bulk elastic constants (solid line).

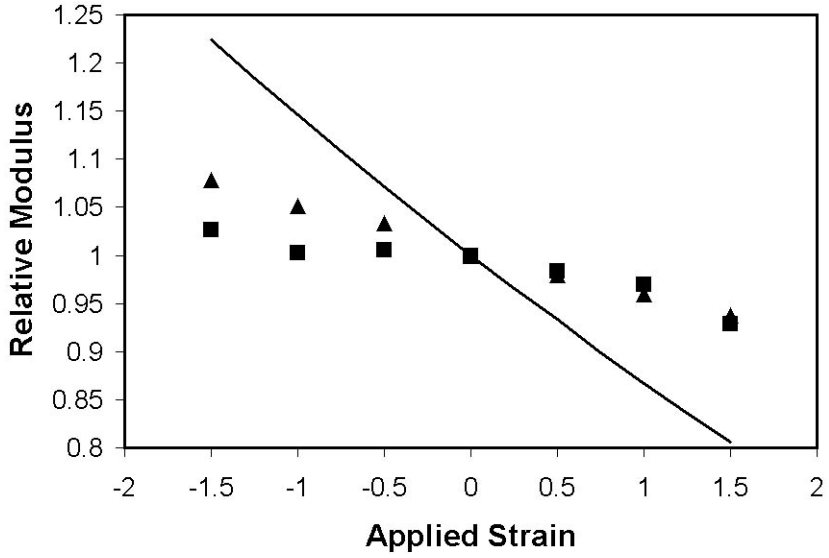

FIGURE 5.11: The relative indentation modulus for a [111] oriented substrate as a function of applied strain for the power law fit to simulated indentation data (triangles), Hertzian calculation using simulated indentation data (squares) and the response expected from the calculation using the bulk elastic constants (solid line).

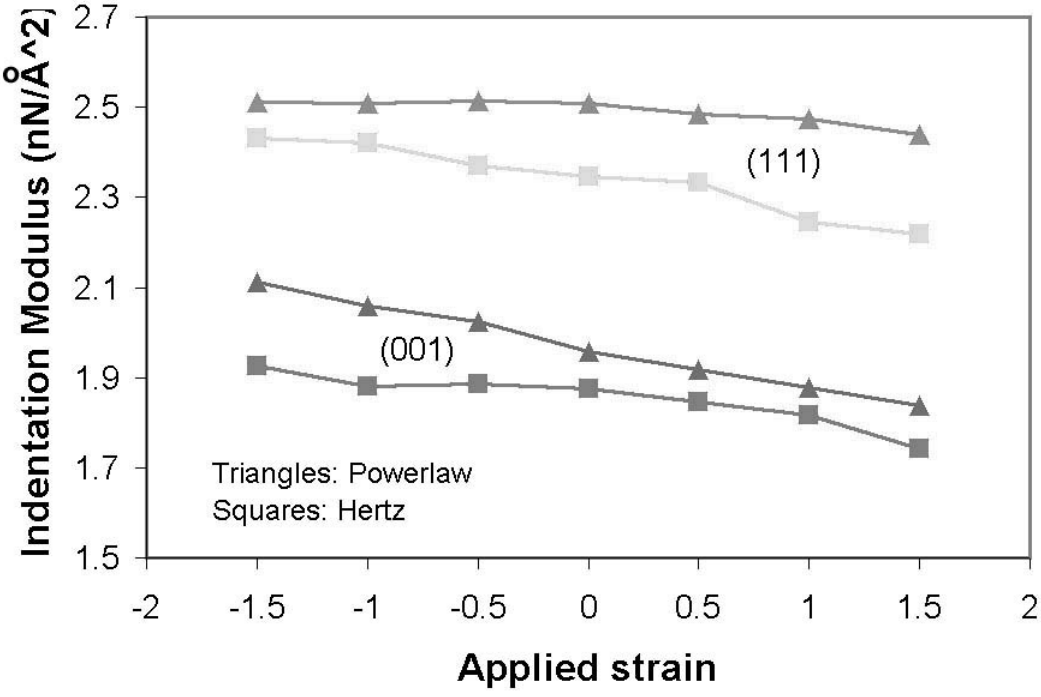

FIGURE 5.12: The indentation modulus for a [001] and [111] substrate as a function of biaxial strain.

5.8 Conclusion

Even though, the simulated nanoindentation experiments suggest the correct dependence of the indentation modulus on the applied strain (compare FIG. 5.12 to FIG. 5.8) the magnitude of this dependence does not match that predicted by using the bulk elastic constants, as shown in FIGS. 5.10 and 5.11. The phenomenological cause for this discrepancy is unclear. It could be that because of the small diameter radius of the indenter the modulus that the indenter 'sees' is not truly the modulus normal to the indentation surface or that the act of indentation relieves the strain locally even though no plasticity is present.

5.9 References

1. D. Wolf, J. Lutsko, and M. Kluge, in *Proceedings of the symposium on "Atomic Modelling in Materials – Beyond pair potentials,"* Chicago IL. 1988. (Plenum, New York).

2. F. Milstein and D. Rasky, "Anharmoncity and symmetry in crystals," *Phil. Mag. A.,* 45, 1982, 49.

3. J.B. Adams, W.G. Wolfer, and S.M. Foiles, "Elastic properties of grain boundaries and their relationship to bulk elastic constants," *Phys. Rev. B.* 40, 1989, 9479.

4. Y. Hiki and A.V. Granato, *Phys. Rev.,* 144, 1966, 411.

5. O.A. Shenderova, J.P. Mewkill and D.W.Brenner, *Molecular Simulation* 25, 2000, 81.

6. J.A. Zimmerman, , C.L. Kelchner, , P.A. Klein, J.C. Hamiltion, and S.M. Foiles, "Surface Step Effects on Nanoindentation" *Phys. Rev. Letts*. 87, 2001, 165507.

7. E.T. Lilleodden, J.A. Zimmerman, S.M. Foiles and W.D. Nix, "Atomistic Simulations of Elastic Deformation and Dislocation Nucleation During Nanoindentation", *J. Mech. Solids*, 51, 2003, 901.

8. D.M. Barnett and J. Lothe, “Line force loadings on anisotropic half-spaces and wedges,” *Phys. Norv.* 8, 1975, 13.

9. J.J. Vlassak and W.D. Nix, “Indentation modulusof elastically anisotropic half spaces” *Phil. Mag. A.* 67, 1993, 1045.

10. J. G. Swadener and G.M. Pharr, “Indentation modulus of elastically anisotropic half-spaces by cones and parabolae of revolution,” *Phil. Mag. A,* 81, 2001, 447.

11. J.J. Vlassak, M. Civarella, J.R. Barber, and X. Wang. “Indentation modulus of elastically anisotropic materials for indenters of arbitrary shape,” *J. Mech. Phys. Sol.* 51, 2003, 1701.

6. AN AD HOC METHOD FOR COUPLING MOLECULAR DYNAMICS SIMULATIONS TO THE CONTINUUM HEAT TRANSFER EQUATION.

In this chapter a new thermostat based on coupling molecular dynamics simulations to the continuum heat equation is presented. The new thermostat is used to predict thermal transport along a pseudo one-dimensional bar of gold modeled using embedded atom potentials. The results are in very good agreement with analytical solution for one-dimensional heat flow. We also use the analytical solution to estimate the thermal diffusivity of EAM gold with no thermostat. The value is determined to be at least five orders of magnitude lower than the reported experimental value - which highlights the need for the new thermostat. To investigate the choice of thermostat on frictional forces we indent a [111] oriented gold surface with a rigid spherical indenter and then slide the indenter along the surface, while recording the normal and friction forces. At low sliding rates the choice of thermostat has little effect on the normal or friction force. As the rate is increased the choice of thermostat has a large effect on the normal and friction forces.

6.1 Background and motivation

In a typical thermostat atomic velocities of the atoms are manipulated to maintain a given temperature. The manipulation can be very simple velocity scaling, or the application of various atomic-level frictional forces (e.g. the Nose-Hoover, Langevin, or Berendson methods) [1]. These thermostats have been developed chiefly to reproduce the natural

temperature fluctuations of individual atoms or regions of atoms and generate the correct ensemble average temperature for the entire system. However these thermostats say nothing about heat flow or thermal transport through the system. In metals thermal properties are determined chiefly from electronic contributions rather than phonons; therefore simulations using analytic potentials that treat electrons with a mean field approach (e.g. the embedded atom method) cannot in general correctly model heat dissipation without some additional constraints on the system. Although there have been attempts to model the influence of electronic degrees of freedom on thermal properties of simulated metals, none of these approaches are completely satisfactory.

6.2 Method

We have developed a new thermostat that couples molecular dynamics simulations to the continuum heat equations so that thermal transport is modeled correctly. In this method the atomic simulation is divided into grid regions or sub-ensembles, and the temperature of each grid region is assigned according to the average kinetic energy of the associated sub-ensemble using the energy relation

$$3/2k_BT = <1/2mv^2> \qquad \text{Eq. 6.1}$$

where k_B is Boltzmann's constant, T is temperature, and where $<1/2mv^2>$ is the average kinetic energy of the sub-ensemble. The continuum heat equation

$$\frac{\partial T}{\partial t} = D\frac{\partial^2 T}{\partial R^2} \qquad \text{Eq 6.2}$$

is then numerically solved using a finite difference method on the grid to predict the new temperature for each grid region,

$$T_{new} = T_{old} + \Delta t D \frac{\partial^2 T}{\partial R^2} \qquad \text{Eq. 6.3}$$

and the atomic velocities are then scaled by

$$v_{new} = v_{old} \sqrt{\frac{T_{new}}{T_{old}}} \qquad \text{Eq. 6.4}$$

in each sub-ensemble to match the continuum solution. The atomic simulation is then carried forward in time by one time step, then new temperatures are calculated, and the continuum heat flow is again solved. These steps are repeated in the simulation, leading to an *ad hoc* feedback between the continuum heat flow and the atomic-scale dynamics. In the equations above the thermal diffusivity D is given by

$$D = \frac{\lambda}{c\rho} \qquad \text{Eq. 6.5}$$

where λ is the thermal conductivity, c is either the heat capacity at constant pressure or volume depending on the simulation ensemble and ρ is the material density. For the straight forward finite difference solution Eq.6.3 of the continuum heat equation Eq.6.2 the maximum step size Δt given by the von Neummann stability criterion required to maintain numerical stability of the algorithm is given by

$$\Delta t \leq \frac{1}{2D\left(1/\Delta x^2 + 1/\Delta y^2 + 1/\Delta z^2 \right)} \qquad \text{Eq.6.6}$$

where Δx, Δy, and Δz are the minimum dimensions of the grid in the x, y, and z directions respectively. For reasonable grid spacing this leads to a maximum time step that is comparable to the time step size of ~0.001 ps typically used in molecular dynamics simulations. For example, for gold λ = 317 W/ m K, at 300 K, c_p = 128 J/m K, and ρ = 19300 kg / m^3 gives a value for the thermal diffusivity of 12831 $Å^2$/ps. With a uniform grid size of $\Delta x = \Delta y = \Delta z$ = 10 Å the maximum time step size is about 0.0012 ps. However, because of the random fluctuations of the atomic velocities and small number of atoms in each sub-ensemble, large fluctuations in the grid temperature may occur from step to step. These large temperature fluctuations reduce the stability of the finite difference algorithm and in practice the time step required to ensure numerical stability is about an order of magnitude smaller than that given by Eq. 6.6. This requires either a smaller molecular dynamics time step or iteration of the finite difference approximation between molecular dynamics steps. Because of the number of grid points is much smaller than the number of atoms, the additional computational cost required for multiple iterations of the finite difference approximation is much smaller than that of reducing the molecular dynamics time step size. Alternatively, larger grids could be used or a more accurate finite difference scheme could be implemented.

This method combines the strengths of both methods, namely full atomistic trajectories from the molecular dynamics not present in the continuum and accurate thermal transport properties from the continuum heat equation not present in the molecular dynamics

simulations. It is important to note that this approach governs heat transport, implicitly including the role of electrons by proper choice of *D*, but not the issue of heat generation at the interface by electronic excitation, a topic of considerable interest, for instance in the study of tribology. In principle it is possible to model these effects at the sliding interface either with less *ad hoc* but more computationally expensive semiclassical methods or with phenomenological models such as the two-temperature method[2,3]. For instance, Ivanov and Zhigilei [3] have presented a method to account for electronic excitation due to laser pulses using the so called two-temperature model. The electronic temperature due to the excitation by the laser pulse is estimated using a finite difference approximation while the molecular dynamics takes care of the phonon interactions. The electronic temperature is then coupled back to the atoms through velocity scaling. The exact amount of kinetic energy and the rate at which it is transferred between the two states is determined using a coupling factor for electron-phonon interactions. Although this method is perhaps more physically realistic, its applicability to a wide range of materials is limited by the knowledge of the constants for the electronic thermal diffusivity term and the coupling of electron-phonon interactions.

6.3 Pseudo one-dimensional heat flow

.To test the validity of the thermostat we simulated pseudo one-dimensional heat flow along a rod of gold modeled using a EAM potential. The atomistic region consists of approximately 45,000 atoms having x, y, and z dimensions of approximately 60, 60, and 200 Å respectively. The simulation space was divided up into sub-ensembles having a uniform size of 20 Å per side giving 3 x 3 x 10 finite difference grids, see FIG. 6.1a. The system was

periodic in the x and y directions and assumed to be insulated at both ends. Using a MD time step size of 0.001 ps, the 200 Å long gold bar was brought to 300 K using a Langevin style thermostat. Once a constant value for potential and kinetic energies were achieved in the bar the Langevin thermostat was turned off. This required approximately 1 ps of simulation time. The finite difference thermostat was then turned on. Ten finite difference iterations (step size of 0.0001 ps) were taken for each 0.001 ps molecular dynamics time step. The values used for the thermal conductivity, heat capacity, and density, obtained from the CRC handbook [4], are for gold λ = 317 W/ m K, at 300 K, c_p = 128 J/m K, and ρ = 19300 kg / m^3. No correction to the finite difference method for the temperature dependence of these values has been made at this time. A thermal gradient was then established along the bar by setting the temperature of atoms within 20 Å of one end of the bar to 600 K by rescaling the atomic velocities to a Gaussian distribution at each time step, FIG. 6.1b.

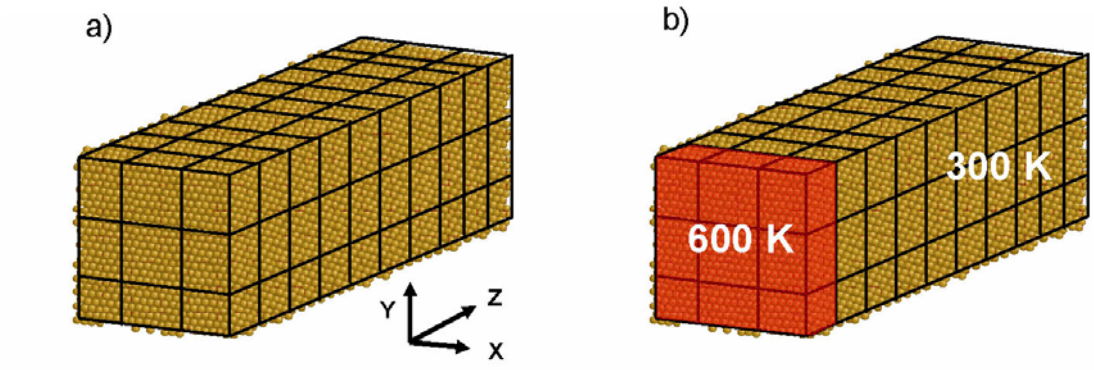

FIGURE 6.1: a) Schematic diagram of the grid set-up for the pseudo one-dimensional heat flow simulation and b) showing the location of the region controlled by the velocity rescaling (shown in red).

The results were then compared to the error function solution to the diffusion equation:

$$T(z,t) = T_i + (T_0 - T_i)(1 - Erf(\frac{z}{2\sqrt{Dt}})) \qquad \text{Eq.6.7}$$

where T(z,t) is the temperature at position z at time t, T_i is the initial temperature, T_0 is the temperature in the heated region, and D is the thermal diffusivity as defined in Eq. 6.5. Plotted in FIG. 6.2 are the average temperature of the atoms in each grid along the z direction of the bar shown in FIG. 6.1 at times t= 0.25 ps, 0.125 ps, and 0.25 ps (squares) and the error function solutions (solid lines). The average grid temperature is in very good agreement with the error function solution. The results of the same simulation with the FD-MD thermostat turned off are shown in FIG 6.3. Again the squares indicate the average grid temperature and the solid line indicates the error function solution. In this case no heat flow is observed.

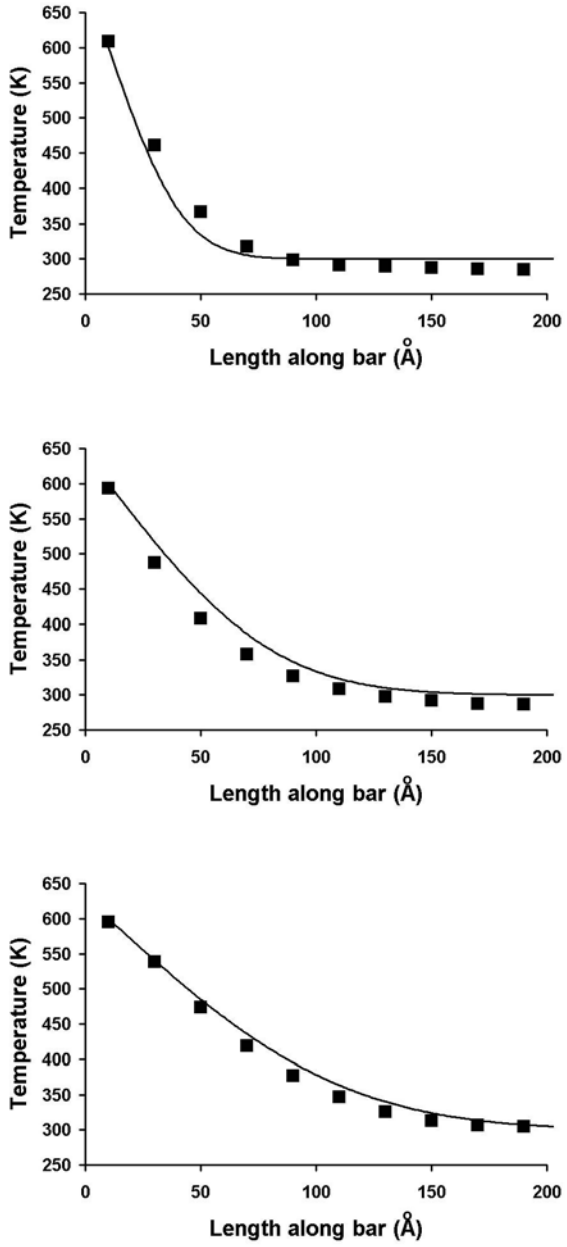

FIGURE 6.2: Average grid temperature (squares) and the error function solution (solid line) as a function of distance along z direction for the bar shown in FIG. 6.1 at $t = 0.025$ ps (top), $t = 0.125$ ps (middle), and $t = 0.25$ ps (bottom) for the case with the FD-MD thermostat turned on.

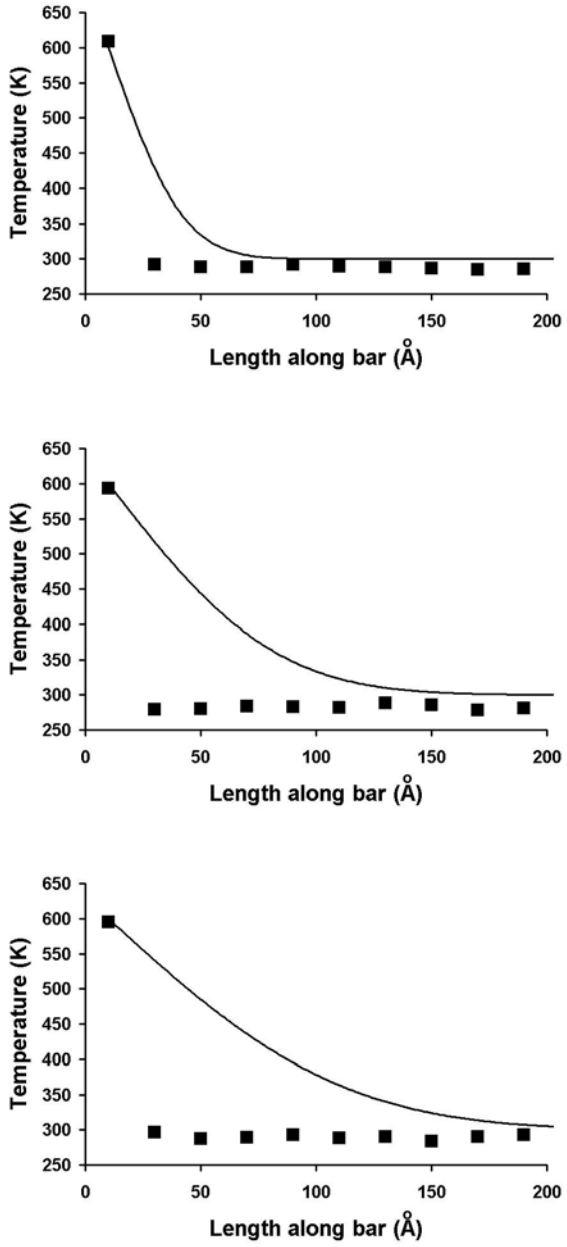

FIGURE 6.3: Average grid temperature (squares) and the error function solution (solid line) as a function of distance along z direction for the bar shown in FIG. 6.1 at $t = 0.025$ ps (top), $t = 0.125$ ps (middle), and $t = 0.25$ ps (bottom) for the case with the FD-MD thermostat turned off.

6.4 Estimation of the thermal diffusivity in EAM gold

We have estimated the value of the thermal diffusivity in EAM gold with no thermostat applied by comparing the temperature profile for heat flow along a pseudo one-dimensional bar of EAM gold to error function solution for heat flow in one dimension. Using a MD time step size of 0.001 ps, the 200 Å long gold bar was brought to 300 K using a Langevin style thermostat. Once a constant value for potential and kinetic energies were achieved in the bar the thermostat was turned off. This required approximately 1 ps of simulation time. A thermal gradient was then established along the bar by setting the temperature of atoms with in 20 Å of one end of the bar to 600 K by rescaling the atomic velocities to a Gaussian distribution at each time step as shown in FIG. 6.1b. The remaining atoms were run with no temperature control. The temperature profile along the bar monitored at every time step. After 100 ps (100,000 MD time steps), no appreciable heat transfer had occurred between the 600 K region and the surrounding atoms and the simulation was ended. Using 100 ps as a lower limit we determined the maximum allowable thermal diffusivity of EAM gold to be no higher than 0.1 $Å^2$/ps by fitting to the analytical solution. This value is at least five orders of magnitude smaller than the experimental value. As a point of reference consider that the thermal diffusivity for a typical polymeric material is around 1-10 $Å^2$/ps. Clearly the EAM method alone is inadequate for modeling thermal transport.

6.5 Effect of thermostat on frictional forces

Conversion of the work associated with a moving interface to heat at the interface is largely responsible for friction in simulations for which there is no plastic damage. In a typical simulation the atomic velocities of atoms buried in the solid away from the solid away from the interface are manipulated to maintain the desired temperature. It has been noted that the choice of thermostat can influence the frictional forces estimated from a simulation because the thermostat controls the rate at which heat is dissipated from a sliding interface [5,6]. If heat dissipation is improperly managed, the results of such studies may or may not be accurate. As we have shown, standard models for metals such as the EAM are inadequate at correctly modeling heat flow and thermal transport. In this section we present two sets of simulations. In these simulations, a rigid tip like that described in Chapter 3 is slid across a gold [111] surface at different sliding rates ranging between 2.5 and 25 Å/ps. In one set of simulations the FD-MD thermostat was used. In the second set of simulations, the thermostat is turned off. The friction force felt by the tip was measured by summing the *x*-component of the forces for all atoms in contact with the tip. The normal force was obtained by summing the *z*-component of forces for all atoms in contact with the tip. A schematic diagram of the set up for the tip sliding experiment is shown in FIG. 6.4. In each simulation the tip was indented to a depth of 2.5 Å before beginning the sliding portion of the simulation.

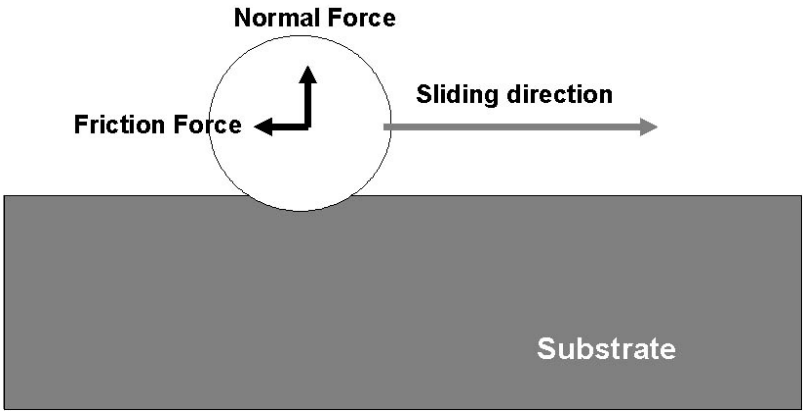

FIGURE 6.4: Schematic diagram for the tip sliding simulations illustrating normal and friction forces felt by the tip.

Shown in FIGS. 6.5 and 6.6 are the normal and friction forces as a function of the sliding distance for a 40 Å radius tip slid across the surface a total distance of 25 Å. Plotted in each figure are the normal and friction forces at sliding rates of 2.5 and 25 Å/ps with the thermostat turned on (T) and off (NT). At the 2.5 Å/ps sliding rate there is little difference between the T and NT force curves. At the higher sliding rate significant differences are apparent between the T and NT force curves. Shown in FIG 6.7 and 6.8 are the average normal and friction forces as a function of sliding rate for rates between 2.5 and 25 Å/ps. Above sliding rates of approximately 10 Å/ps, the choice in thermostat has a very strong effect on the average normal and friction forces. The plot shown in FIG. 6.9 shows average surface temperature as a function of simulation time for the T and NT cases at sliding rates of 2.5 and 25 Å/ps. This plot suggests that there is significant heating occurring beneath the tip in the NT simulation at the higher sliding rate. With the thermostat turned on this heat is rapidly removed from the surface. As the temperature increases, the bonds are softened and atoms are more easily pushed out of the way by the moving tip. This results in a lower

normal and friction forces. When the FD-MD thermostat is used surface temperature does not increase as rapidly which results in higher normal and friction forces.

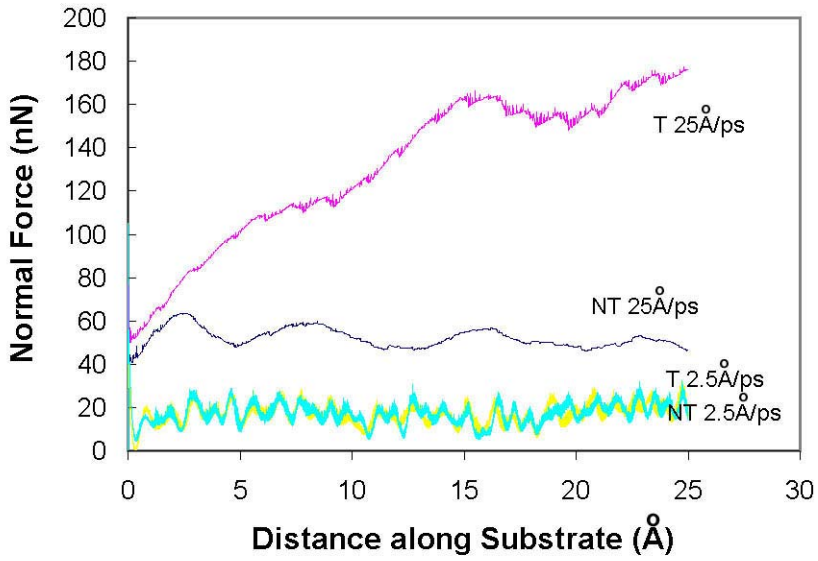

FIGURE 6.5: Normal force as a function of sliding distance. T indicates that the FD-MD thermostat is turned on. NT indicates that there is no thermostat.

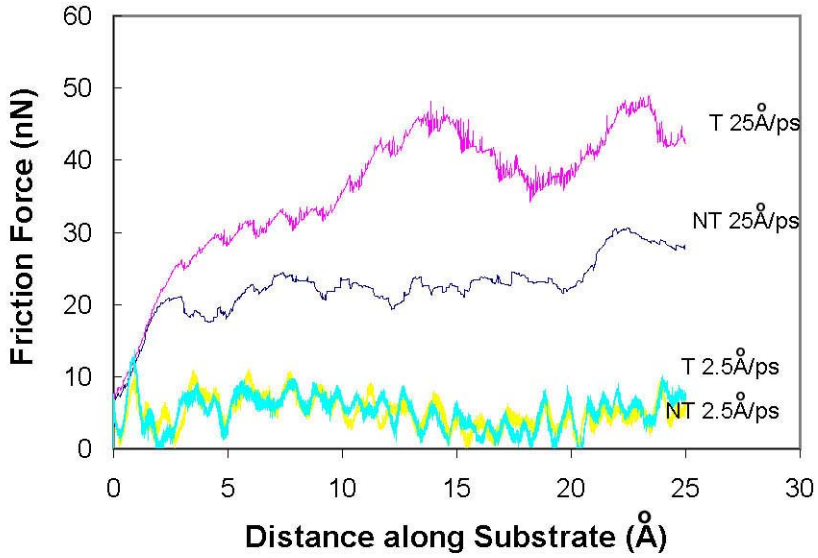

FIGURE 6.6: Friction force as a function of sliding distance. T indicates that the FD-MD thermostat is turned on. NT indicates that there is no thermostat.

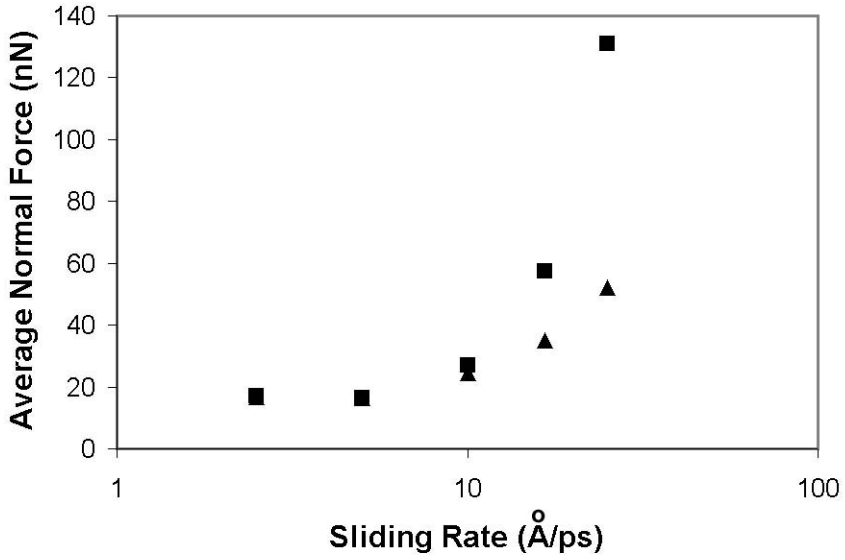

FIGURE 6.7: Average normal force as a function of sliding rate for FD-MD thermostat (squares) and with no thermostat (triangles).

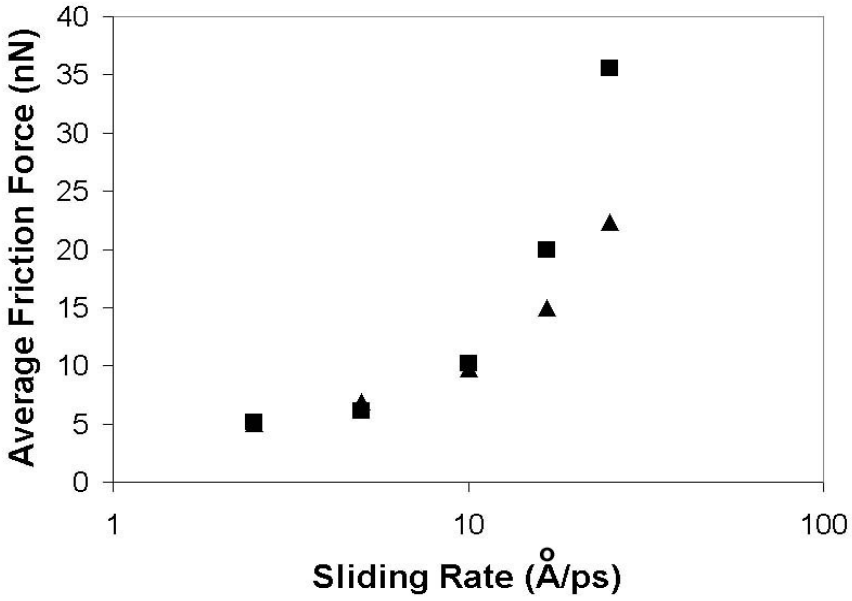

FIGURE 6.8: Average friction force as a function of sliding rate for the FD-MD thermostat (squares) and with no thermostat (triangles).

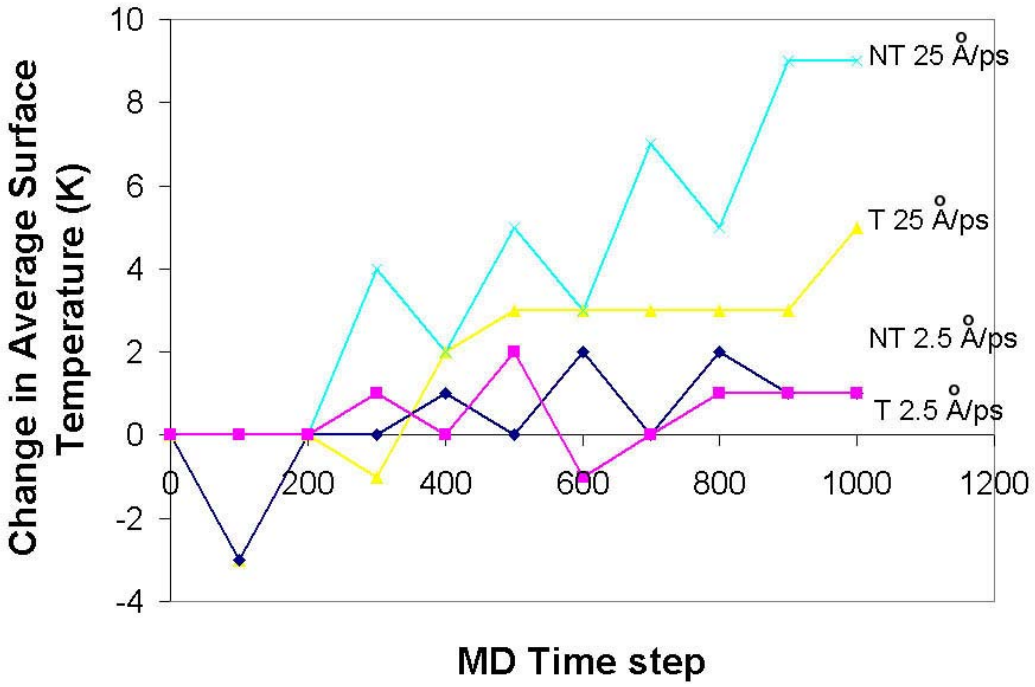

FIGURE 6.9: Change in the average surface temperature as a function of MD time step at rates of 2.5 and 25 Å/ps. T indicates that the thermostat was turned on. NT indicates that there was no thermostat.

6.6 Summary

The proposed thermostat has several advantages over prior thermostats used in molecular simulations. First, the experimental thermal conductivities and heat capacities can be used rather than relying on the simulation to reproduce a correct thermal response. As discussed above, as we have shown this is especially important for metals. Similarly, with a grid based finite difference solution temperature dependent conductivities and heat capacities can be used, with their values depending on the temperature of a given grid region [7]. Second the grid region can extend beyond the boundaries of the atomic simulation, and with some modification to the finite difference solution, the dimensions of the grid regions can be

increased to match macroscopic-scale boundary conditions. This allows scaling between atomistic and engineering length scales. Third, in principle, the effect of bulk defects such as dislocations and grain boundaries on heat transfer can be incorporated into the model by making the appropriate changes in thermal properties around these defects. Hence coupling of plastic damage to friction via heat dissipation can be modeled. Finally the atomic dynamics that generate heat at the interface can be straight forwardly replaced with a phenomenological heat flux vector, and the grid coarse grained using these rates to produce heat transfer dynamics over longer length and time scales according to the time scaling of Eq. 6.4.

6.7 References

1. J.A. Harrison, S.J Stuart, and D.W. Brenner, "Atomic-scale simulation of tribological and related phenomena," Chapter 10 in the CRC Handbook of Micro/Nanotribology, Second Edition, Bushan, ed. (CRC Publishers, 1998). pp. 525-596.

2. Tully, J.C. "Chemical dynamics at metal surfaces' *Ann. Rev. Phys. Chem.* 51, 2000, 153.

3. D.S. Ivanov and L.V. Zhigilei, "Combined atomistic-continuum modeling of short-pulse laser melting and disintegration of metal films," *Phys. Rev. B*, 68, 2003, 064114.

4. CRC Handbook, (CRC Publishers)

5. G. He, and M.O. Robbons, "Simulations of the static friction due to absorbed molecules," *Phys. Rev. B*. 64, 2001, 35413.

6. M.S. Tomassone, J.B. Sokoloff, A. Widom, and J. Krim, "Dominance of phonon friction for a xenon film on a silver (111) surface," *Phys. Rev. Lett.* 79, 1997, 4798.

7. B.S. Yilbas, "Numerical approach to pulsed laser heating of a semi-infinite aluminum substance," *Heat and Mass Trans.* 31, 1996, 279.

7. CONCLUSIONS AND FUTURE WORK

In chapters four and five, the relationship between pre-existing stress in the substrate material and indentation modulus has been investigated. We have shown that for indentations where plasticity is present, the modulus is independent of the pre-existing stress level when the correct contact area is used. The simulations show that large errors in the modulus are possible when using the empirical estimates for contact area commonly used in nanoindentation experiments. The simulation results for the modulus calculation are in very good agreement with the experimental results of Tsui, Pharr, and Oliver [1], and those of Sines and Carlson[2] for macroscale indentations suggesting that this effect occurs over a wide range of length scales. However, the results for hardness calculated using the correct areas were different than those presented in Tsui, Pharr, and Oliver's work. Our work suggests a dependence of hardness on the pre-stress level. At present this behavior is unexplained. One possible explanation of this difference could lie in the differences observed in the plastic deformation generated at the different levels of the pre-stress. Further work, perhaps though the use of finite element analysis, in this area needs to be conducted to sort out these details. When the pre-stressed substrates were indented elastically, we observed a dependence of modulus on the pre-stress level. This dependence qualitatively matched the expected dependence as calculated using bulk elastic constants; however the magnitude of the dependence was not in good agreement.

The assumption that the indentation modulus reduces to $E_{R(hkl)} = \frac{E_{(hkl)}}{1-\nu_{(hkl)}^{2}}$ for axisymmetric-anisotropic materials assumes that the depth of the indentation is very small relative to the radius of the indenter so that the contact angle defined as the angle

between the surface and the indenter at the edge of contact is very small [3]. For an indenter with a 40 Å radius indented to a depth of 2.5 Å, the contact angle is approximately 20 degrees. Increasing the indenter radius to 100 Å only decreases the contact angle to 12 degrees. Either more complex elastic analyses that deviate from the axisymmetric-anisotropic assumption or much large indenters would be required to predict the correct magnitude of the dependence of modulus on the pre-stress level.

In our model we took our substrate material to be gold and mimicked a hard under layer by including rigid atoms at the bottom of the simulation box. Then we modeled strain by modifying the periodic boundary conditions. This is meant to approximate a soft thin film on a hard substrate. However, it ignores important substrate-film interactions which may modify the results significantly. A better atomistic approach may allow these interactions to be included. The modified embedded atom method first developed by Baskes [4] includes an angular term that allows a much wider range of materials to be modeled. It is particularly well suited to modeling silicon [5]. With some modification (namely the development of pair potentials between dissimilar atoms) it is possible to model a wide range of alloys. A recently developed modified embedded atom method potential for silicon and gold [6] could allow a more detailed analysis of the substrate-film interactions offering an interesting extension to the work presented here in Chapters 4 and 5. With the Si-Au potential it would be possible to study, from an atomistic point of view, the effect of film thickness and residual stress on the interpretation of nanoindentation data. In addition, a number other points of interest could be investigated. For instance, during nanoindentation of thin films, the film may fracture, the film may delaminate from the

substrate, and the indenter may indent through the film and into the substrate. It would be useful to obtain an atomistic picture of these mechanisms.

Incorporation of grid-based finite difference methods into molecular dynamics simulations is a relatively new research area rife with possibilities. In chapter 6, we showed the utility of such a combination to provide a solution to a problem inherent to molecular dynamics simulations in metals, namely that of correctly modeling heat flow and thermal transport. In this combined method, full atomistic trajectories are represented by the molecular dynamics and accurate thermal transport properties are included by the continuum heat equation. The model presented here makes several assumptions that could be improved upon in future versions. First, the temperature dependence of the heat capacity, thermal conductivity, and density are neglected in this simple model. These should be included in future models. Second, latent heats for phase transformations are not included. Without the latent heat, melting and vaporization cannot be correctly modeled and the model is valid only for temperatures less than the melting point of the material. One solution to this problem is to generate grid based reservoirs for heat that depend on the amount of each phase present in the grid at any given time [7]. In the case of a solid-liquid phase transformation, this would allow atoms contained in a grid region undergoing a phase transformation to absorb heat from neighboring grids without changing the temperature in the grid until the melting is completed, thus mimicking a first order phase transformation. The combination of grid-based methods with molecular dynamics simulations is not limited solely to thermal transport. One might also apply such methods to modeling the effects of electrical and

magnetic fields or diffusion by incorporating the appropriate fundamental equations. For example, the US Navy[8] is interested in implementing electro-magnetic rail guns on their ships. Rail guns are attractive because they require no chemical-propellant to launch their projectile. This gives the Navy the ability to carry more projectiles and makes the ships safer for the sailors. The largest hurtle to implementing these weapons are the reusability of the rails and armature of the guns. Due to the extremely high velocity of the armature (up to 3000-10000 m/s) there are significant friction effects and because of, the high electric fields and currents, arcing and plasma may form between the rails and armature leading to pitting of the rails. This makes repeated firing difficult. By implementing concurrent grid based methods for the magnetic fields, electrostatic potentials, and heat flow with full atomistic simulations, it might be possible to achieve a fuller understanding of the physics involved during discharge of the rail gun.

7.1 References

1. T.Y. Tsui, W.C. Oliver and G.M. Pharr, *J. Mater. Res.* 11, 1996, 752.

2. G. Sines and R. Carlson, *ASTM Bulletin.* 180, 1952, 35.

3. J. G. Swadener and G.M. Pharr, "Indentation modulus of elastically anisotropic half-spaces by cones and parabolae of revolution," *Phil. Mag. A,* 81, 2001, 447.

4. M.I. Baskes, "Modified Embedded atom potentials for cubic materials and impurities," *Phys. Rev. B.* 46, 1992, 2727.

5. M.I. Baskes, "Application of the embedded atom method to covalent materials: A semiempirical potential for silicon," *Phys. Rev. Letts.* 59, 1987, 2666.

6. Kuo CL, Clancy P "MEAM molecular dynamics study of a gold thin film on a silicon substrate", Surf. Sci. 55, 2004, 39.

7. B.S. Yilbas, "Numerical approach to pulsed laser heating of a semi-infinite aluminum substance," *Heat and Mass Trans.* 31, 1996, 279.

8. W. A. Walls, W. F. Weldon, S. B. Pratap, M. Palmer, and Lt. David Adams, "Application of Electromagnetic Guns to Future Naval Platforms", 1998.

APPENDIX A: THE INSCRIBED POLYGON CALCULATION

A.1 Method

The basic method for determining the projected contact area in the nanoindentation simulations conducted in this work is given below. The description assumes that the indentation axis is normal to the x-y plane, see FIG. A.1.

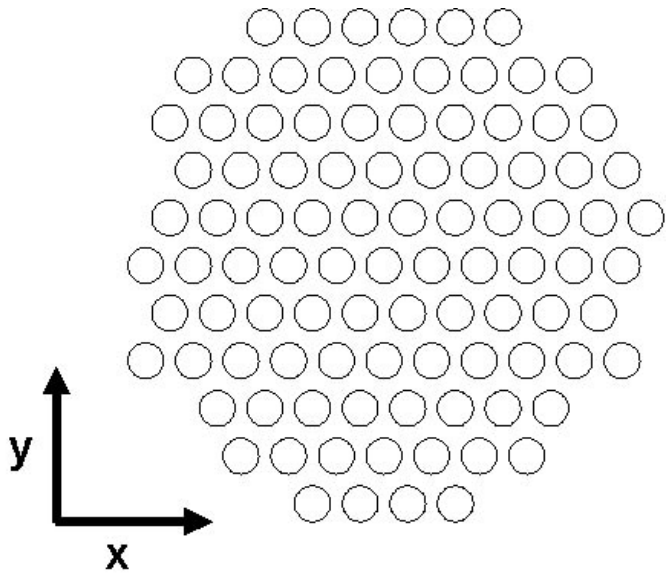

FIGURE A.1: Schematic of diagram showing contacted atoms showing orientation of x and y axes.

First a list of all contacted atoms and their spatial coordinates is generated using the criterion for contact. As described in Chapter 3, for both the repulsive potential indenter and the rigid indenter contact is defined as $R_{il}<R$ where R_{il} is the radial distance from the

center of the indenter to atom i and R is the radius of the indenter. This data may be collected at each molecular dynamics time step or some other user defined interval, depending on the desired accuracy of the measurement. Given a set of atomic coordinates describing the contact (one time snapshot), the contact area may then be determined as follows:

1. The maximum and minimum values of the edges of the contact area determined in both the x and y directions, FIG. A.2.

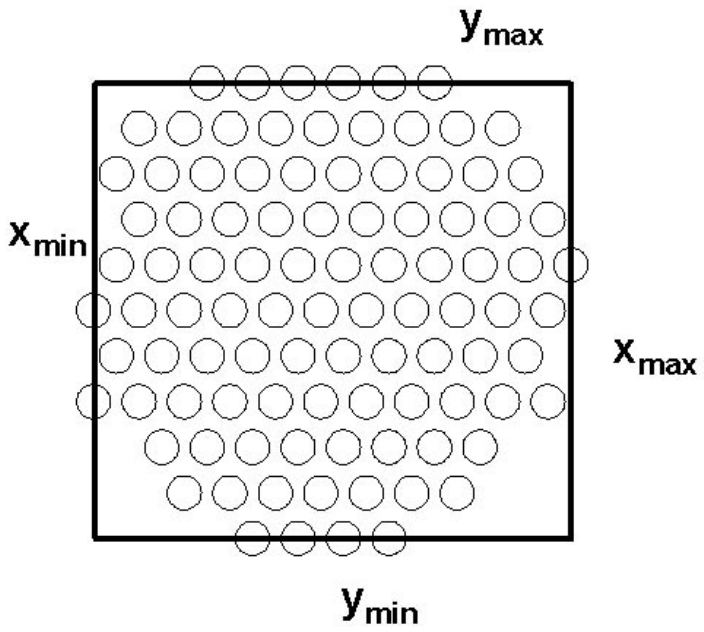

FIGURE A.2: Maximum dimensions of the contact in the x and y directions.

2. The total possible area of the contact is taken as the area of the rectangle determined as $(x_{max}-x_{min})*(y_{max}-y_{min})$. Then the rectangle defined by the maximum and minimum dimensions of the contact is subdivided into grids, separately for the x and y dimensions.

The grid size is on the order of the interatomic spacing as shown in FIG. A.3. For a FCC lattice this value is given as $\sqrt{3}/3\,a_0$ where a_o is the lattice parameter.

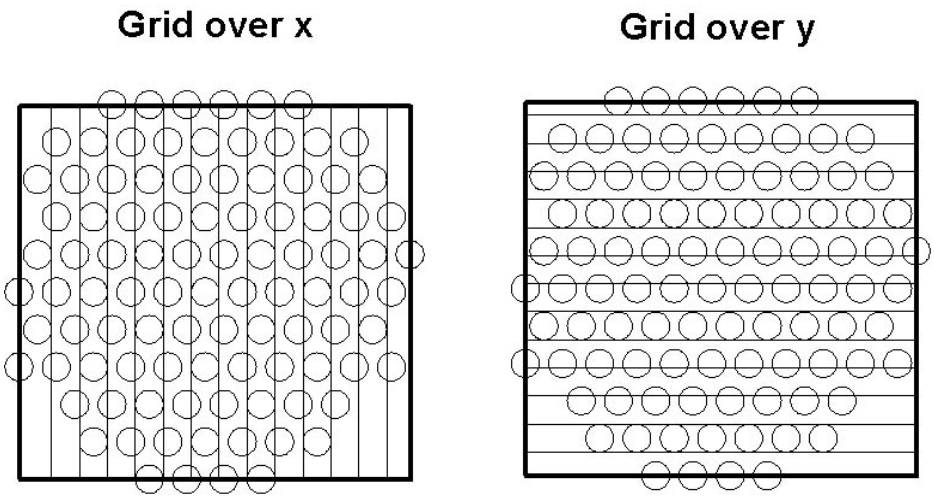

FIGURE A.3: Separate grids for x and y directions.

3. The maximum and minimum values of the y coordinates of all the atoms contained in each x grid are determined, FIG. A.4. These coordinates are saved and used to generate a set of trapezoids between the maximum and minimum y coordinates in adjacent grids, FIG. A.5.

4. The areas of each trapezoid are subtracted from the total area determined in step 2. This gives the area inscribed by this set of points.

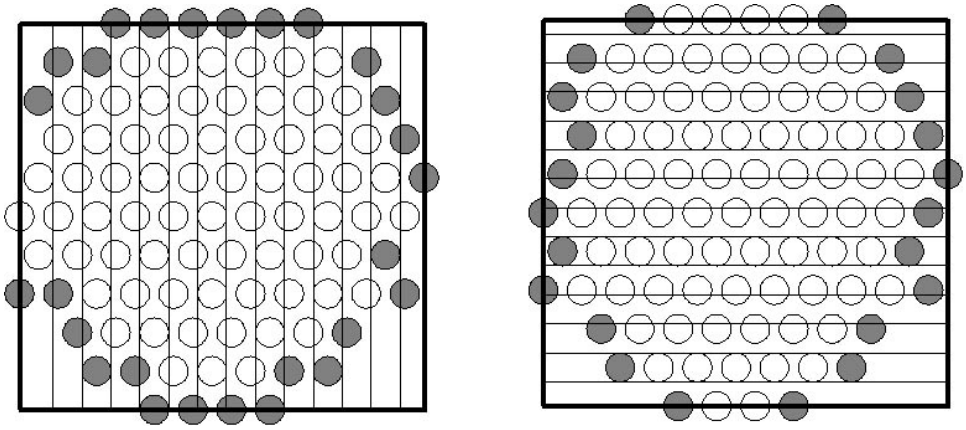

FIGURE A.4: Highlighted atoms are the maximum and minimum values of the y coordinates of atoms contained in each x grid. (left), and the maximum and minimum values of the y coordinates of atoms in each y grid (right).

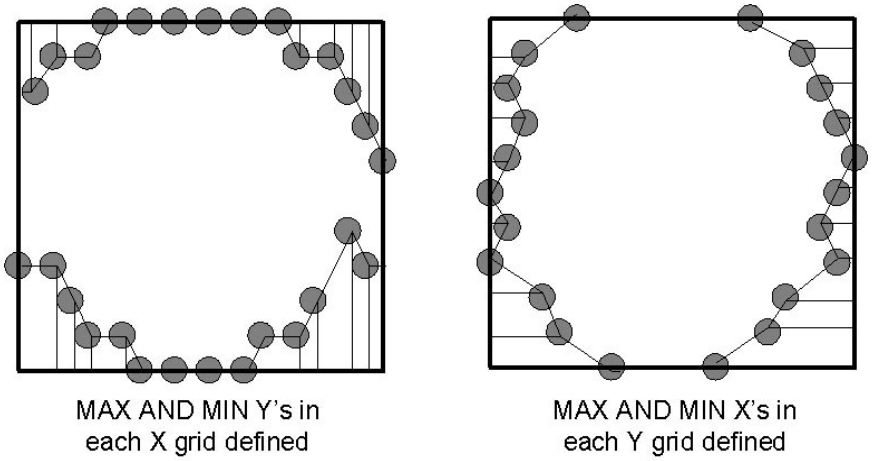

FIGURE A.5: The trapezoids created by connecting the maximums and minimums in adjacent grids. The area of each trapezoid is subtracted from the total area of the rectangle to determine the area inside the polygon described by these points.

5. Steps 3 and 4 are repeated for the y grid.

6. The areas determined in steps 4 and 5 are averaged. This is taken to be the contact area of the polygon inscribed by the outer ring of contacted atoms, FIG A.6.

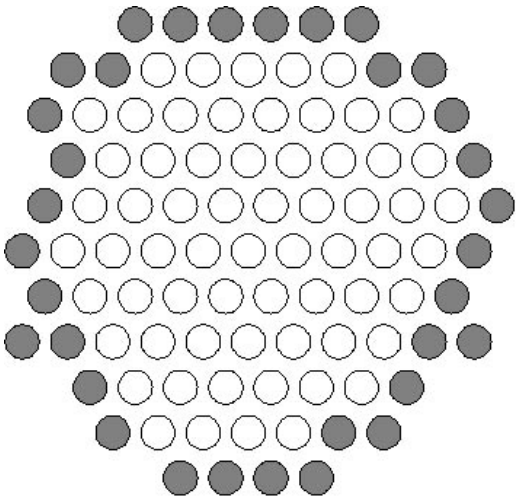

FIGURE A.6: Polygon inscribed by the ring of atoms at the perimeter of the contact.

A.2 FORTRAN source code

```
* Program to calculate projected area under indenter
* Reads xyz formatted input file.

      implicit real (a-h,o-z)
      dimension r0(3,10000),f(10000)
      dimension nbinx(2,10000),nbiny(2,10000)
      character*15 atype
      character*15 filename
* initiallize max and min values
      xmax=-10000.
      xmin=10000.
      ymax=-10000.
      ymin=10000.

* read data
      write(*,*) 'Enter unitcell filename:'

      read(*,*) filename

      write(*,*) filename
      Open(11,file=filename,status='unknown')
      Open(12,file='out.xyz',status='unknown')
      open(13,file='area.d',status='unknown')

      write(*,*) 'enter number of frames to read:'
      read(*,*) nframes

      npmax=-10000
      do n=1,nframes
        read(11,*) np
```

```
        read(11,*)
            do i=1,np
              read(11,*)
            enddo
            npmax=max(np,npmax)
      enddo
      close(11)
      Open(11,file=filename,status='unknown')

      do n=1,nframes
      ftot=0
        read(11,*) np
        read(11,*)
        if(np.eq.0) goto 10

        do i=1,np
          read(11,*) atype,r0(1,i),r0(2,i),r0(3,i),f(i)
          ftot=ftot+f(i)
          if(r0(1,i).gt.xmax) then
            xmax=r0(1,i)
            nbxu=i
          endif
          if(r0(2,i).gt.ymax) then
            ymax=r0(2,i)
            nbyu=i
          endif
          if(r0(1,i).lt.xmin) then
            xmin=r0(1,i)
            nbxl=i
          endif
          if(r0(2,i).lt.ymin) then
            ymin=r0(2,i)
            nbyl=i
          endif
        enddo

        write(*,*) 'x min, max: ',xmin,xmax
        write(*,*) 'y min, max: ',ymin,ymax

        ave=(abs(xmin)+abs(ymin)+xmax+ymax)/4.
        nbins = nint(ave-1.)
        write(*,*) 'ave,nbins', ave, nbins

        binsizex = (xmax-xmin)/nbins
        binsizey = (ymax-ymin)/nbins

* set upper and lower bins to max and min coord #
        nbinx(1,1)=nbxl
        nbinx(2,1)=nbxl
        nbiny(1,1)=nbyl
        nbiny(2,1)=nbyl
        nbinx(1,nbins+2)=nbxu
        nbinx(2,nbins+2)=nbxu
        nbiny(1,nbins+2)=nbyu
        nbiny(2,nbins+2)=nbyu

* find max x in y bin and vice versa
```

```
        do i=1,nbins
          binxl=float(i-1)*binsizex+xmin
          binxu=float(i)*binsizex+xmin
          binyl=float(i-1)*binsizey+ymin
          binyu=float(i)*binsizey+ymin
*     reset values
          xbmax=-10000.
          xbmin=10000.
          ybmax=-10000.
          ybmin=10000.

          do j=1,np
*     columns (ymaxs and ymins)
            if((r0(1,j).ge.binxl).and.(r0(1,j).le.binxu)) then
              if(r0(2,j).ge.ybmax) then
                ybmax=r0(2,j)
                nbinx(2,i+1)=j
              endif
              if(r0(2,j).le.ybmin) then
                ybmin=r0(2,j)
                nbinx(1,i+1)=j
              endif
            endif

*     rows (xmaxs and xmins)
            if((r0(2,j).ge.binyl).and.(r0(2,j).le.binyu)) then
              if(r0(1,j).ge.xbmax) then
                xbmax=r0(1,j)
                nbiny(2,i+1)=j
              endif
              if(r0(1,j).le.xbmin) then
                xbmin=r0(1,j)
                nbiny(1,i+1)=j
              endif

            endif
          enddo ! j loop
        enddo ! i loop

* calculate areas
        atot=(xmax-xmin)*(ymax-ymin)


        at=0.
        ab=0.
        al=0.
        ar=0.

        do i=1,nbins+1

*     top
          x1=r0(1,nbinx(2,i))
          x2=r0(1,nbinx(2,i+1))
          y1=ymax-r0(2,nbinx(2,i))
          y2=ymax-r0(2,nbinx(2,i+1))
          at=at+0.5*(x2-x1)*(y2+y1)
*     bottom
```

```
          x1=r0(1,nbinx(1,i))
          x2=r0(1,nbinx(1,i+1))
          y1=r0(2,nbinx(1,i))-ymin
          y2=r0(2,nbinx(1,i+1))-ymin
          ab=ab+0.5*(x2-x1)*(y2+y1)
*     left
          x1=r0(1,nbiny(1,i))-xmin
          x2=r0(1,nbiny(1,i+1))-xmin
          y1=r0(2,nbiny(1,i))
          y2=r0(2,nbiny(1,i+1))
          al=al+0.5*(x2+x1)*(y2-y1)
*     right
          x1=xmax-r0(1,nbiny(2,i))
          x2=xmax-r0(1,nbiny(2,i+1))
          y1=r0(2,nbiny(2,i))
          y2=r0(2,nbiny(2,i+1))
          ar=ar+0.5*(x2+x1)*(y2-y1)

        enddo

* finish area calcs and output
        Ax=atot-at-ab
        Ay=atot-al-ar
        Ave=0.5*(ax+ay)
              write(*,*) 'ax,ay,ave: ',ax,ay,ave
              write(*,*) 'ftot,Pm', ftot,ftot/ave
              write(13,*) n,np,ax,ay,ave,ftot,ftot/ave

        write(12,*) npmax
        write(12,*) ' '

        do i=1,np
            write(12,200) r0(1,i),r0(2,i),r0(3,i),f(i)
        enddo

* Load up a dummy atom for chime file
        do i=np+1,npmax
            write(12,200) r0(1,np),r0(2,np),r0(3,np), 0.0
        enddo

      xmax=-10000.
      xmin=10000.
      ymax=-10000.
      ymin=10000.

 10   continue
      enddo

      close(11)
      close(12)

 100  format('Pt',3f12.4)
 150  format('Ag',3f12.4)
 200  format('Au',4f12.4)

      end
```

APPENDIX B. DATA VISUALIZATION TECHNIQUES

The simulations in this thesis often required dealing with and visualizing large sets of data. For instance, the positional data of the 960,000 atom simulations presented in Chapter 4 required approximately 36 Mb of storage space for each time snapshot, with correspondingly large file sizes for the atomic velocities and stresses. A typical nanoindentation simulation consisted of 4000 time steps. Storage of the entire set of positions, velocities, and stresses was not feasible and judicious choices were made as to what data should be stored for later use; usually this amounted to storing data every 500 time steps or so. This captured the key steps in the indentation such as the nature of the contact at the peak load and the residual contact impression after the load was removed. Once the data was collected and stored it was still a challenge to manipulate it and visualize it. Typically coordinate data was visualized using a freeware internet browser plug-in known as MDL: CHIME (http://www.mdlchime.com). CHIME takes the Cartesian coordinate data representing atomic positions and translates it into a visual display of the atoms. In addition to mapping x, y,z data, CHIME is capable of mapping a fourth parameter to each atom through coloration. The program has its limitations, however. Above approximately 100,000 atoms visualization becomes cumbersome and slow. It is also difficult to see inside the material, for instance to see dislocations. The purpose of this appendix is to provide a review of some of the methods developed to parse and visualize the large data sets.

B.1 Sectioning

Perhaps the most obvious method of visualization particularly to the material scientist is cross-sectioning. In this method, the set of maximum and minimum coordinates for the area of interest are defined and all coordinates outside of this region are excluded, as illustrated in FIG B.1. The resulting data set is just a fraction of size of the total data set and is easily visualized.

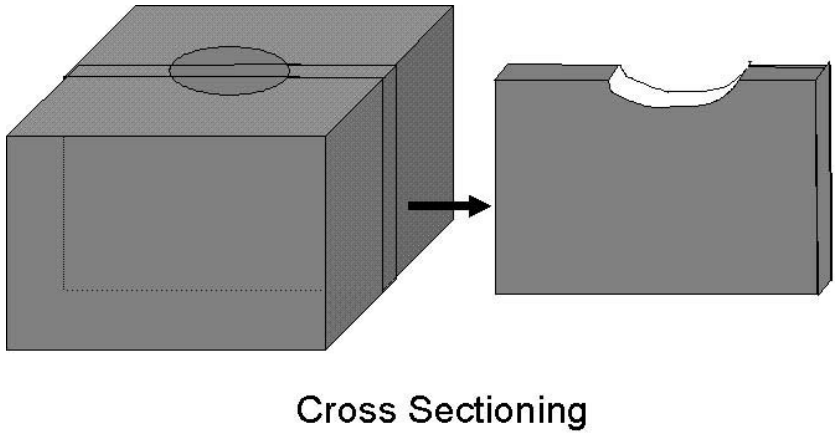

FIGURE B.1: Schematic of a cross-section. Material outside the area of interest is removed.

B.2 Coordination number

Another useful and fairly simple method for analyzing and visualizing coordinate data is through the calculation of each atom's coordination number. Coordination number is simply the number of first nearest neighbors local to a single atom. The number of neighbors for a given atom is tallied by calculating the radial distance between the atom and all other atoms and counting only atoms that have radial distances less than the average of the first and

second neighbor distances. For a perfect FCC lattice the number of nearest neighbors is twelve. Different defect structures will have different coordination numbers; for instance a (111) surface will have a coordination number of nine. By coloring atoms according to the coordination number it is possible to visualize any defects present including surfaces, dislocations, point defects and grain boundaries. The atoms with coordination number corresponding to the perfect lattice can be removed to generate a clearer picture of the interior defects. Not all defects can be highlighted using a coordination number analysis. For instance in FCC materials, stacking faults cannot be distinguished from the perfect material. The faulted region has a HCP structure which also has a coordination number of twelve.

B.3 The centrosymmetry parameter

Centrosymmetric materials remain centrosymmetric under elastic strain. In a centrosymmetric material each atom has pairs of equal and opposite bonds to its nearest neighbors. With elastic distortion these bonds will change direction and length but will remain equal and opposite. This relation no longer holds in the case of defected materials. The centrosymmetry parameter for atom i defined for an FCC lattice with 12 nearest neighbors j is

$$P_i = \sum_{j=1,6} \left| R_{ij} + R_{ij+6} \right|^2 \qquad \text{Eq. B.1}$$

where $\mathbf{R}_{ij}$ and $\mathbf{R}_{ij+6}$ are the bond vectors corresponding to pairs of atoms[1]. The parameter P equals 0 for elastically deformed materials and is non-zero for plastically deformed materials. The summation from 1 to 6 indicates summation over the 6 pairs of opposite atoms in the FCC lattice, see FIG B.2.

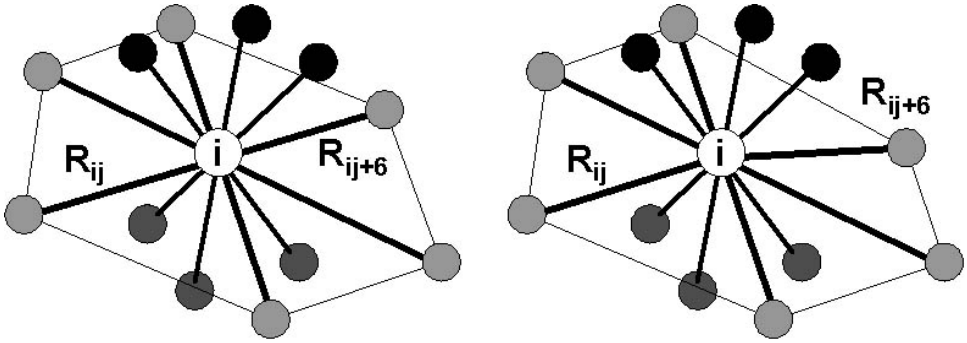

FIGURE B.2: Illustration of atomic pairs about a central atom i. On the left $\mathbf{R}_{ij}+\mathbf{R}_{ij+1}=0$. On the right $\mathbf{R}_{ij}+\mathbf{R}_{ij+1}\neq 0$.

The algorithm for calculating the centrosymmetry parameter is as follows:

1. Find neighbors for all atoms i using an order-n binned neighbor search.
    a. While finding neighbors, store bond vector $\mathbf{R}_{ij}$ for each neighboring atom
2. Create a pair list for each atom i by finding minimum value of the vector sum between atom j and atom k where atoms j and k are neighbors of i.
3. Once the pairs are determined the centrosymmetry parameter is calculated using Eq. B.1. The values of centrosymmetry parameter for various types of defects in FCC crystals are as follows:

4. Typically some tolerance is specified as a cut-off for the centrosymmetry parameter and all atoms with parameter values greater than the cut-off are output.

Typical values for the centrosymmetry parameter are:

Perfect lattice: 0.0

Surface atom: 24.97

Vacancy (or stacking fault): 8.32

Partial dislocation: 2.1

B.4 The slip vector parameter

To determine information on the Burger's vector of dislocations, Zimmerman *et al*[2] developed an expression for the slip vector, defined as:

$$s^{\alpha} = -\frac{1}{n_s}\sum_{\beta\neq\alpha}^{n}\left(R^{\alpha\beta} - R_o^{\alpha\beta}\right) \qquad \text{Eq. B.2}$$

Coordinates from two different points in time can be compared using the slip vector parameter. In this method, coordinate data obtained during the simulation is compared to some reference coordinate data. Usually the initial set of coordinates is used for the reference state. This allows deformation to be tracked throughout the simulation as a function of time. In Eq. B.2, n is the number of nearest neighbors of atom α in the reference material, n_s is the number of neighbors in the deformed material (taken during or after simulation), $R^{\alpha\beta}$ is the vector difference between atom α to atom β in the deformed position and $R_o{}^{\alpha\beta}$ is the vector difference in the reference material. The slip vector can be used for

any microstructure regard less of symmetry making it more useful than the centrosymmetry parameter described above.

The basic algorithm is as follows:

1. For all atoms α in the reference lattice, determine nearest neighbors and vector differences $R_o^{\alpha\beta}$ between atom α and its neighbors β.
2. Determine the number of nearest neighbors in the deformed material.
3. Determined the vector differences $R^{\alpha\beta}$ between atom α and its neighbors β in the deformed material using the neighbor list generated for the reference structure.
4. Evaluate Eq. B.2.
5. Typically some tolerance is specified as a cut-off for the minimum slip vector and all atoms with parameter values greater than the cut-off are output as 'slipped' atoms.

B.5 Some notes on determination of nearest neighbors

Analyses using the coordination number, centrosymmetry, and slip vector parameters all require the determination of the nearest neighbors for each atom. Often a 'brute force' approach is used to do this. This requires that all atoms j are checked against atoms i to see if they are close enough to be neighbors. This is an order N^2 operation, where n is the number of atoms. For a few hundred atoms this is a reasonable method and very simple to code; see the pseudo code in FIG B.3. Increase the number of atoms to a few thousand or a few hundred thousand atoms and the time required to simply analyze the data becomes enormous.

```
Do i=1,natoms-1
      Do j=i+1,natoms
            Calculate Rij
            If Rij < Rcutoff then atom j=neighbor of atom i
      Enddo
Enddo
```

FIGURE B.3: Pseudo code for a 1/2N(N-1) 'brute force' neighbor search.

An alternative method for determining in neighbors is the cell index method or binned neighbor list [3]. In this method the simulation box is divided up into N_{bins} with a size equal to some cut-off value. In an MD simulation the cut-off is slightly larger than the cut-off of the potential function. The analyses presented here use the average of the first and second neighbor distances as the cut-off. Next a list of atoms contained in each box is established. Searching for neighbors is then a simple matter of searching only over the $N_c = N/N_{bins}$ atoms contained in adjacent bins. The basic algorithm is shown by the pseudo code in FIG. B.4. In three dimensions this method is approximately of the order $27N*N_c$.

```
* Find number of bins in each direction
Nbinx = box length of x / (rcutoff+small)
Nbiny = box length of y / (rcutoff+small)
Nbinz = box length of z / (rcutoff+small)

* assign atoms to bins
do i=1,natoms
      ix = R(1,i)/rcutoff
      iy = R(2,i)/rcutoff
      iz =  R(3,i)/rcutoff
*     bin number for atom i
      bin (i) =(iz-1)*nbinx*nbiny+(iy-1)*nbinx+ix
enddo

do i = 1,natoms
      ix = R(1,i)/rcutoff
      iy = R(2,i)/rcutoff
      iz = R(3,i)/rcutoff

* Loop over the 27 neighboring bins

      do ii=ix-1,ix+1
        do jj=iy-1,iy+1
            do kk=iz-1,iz+1
              ib = (kk-1)*nbinx*nbiny+(jj-1)*nbinx+ii
              do for all atoms j in bin ib
                  if j≠i, Calculate Rij
                  If Rij < Rcutoff then atom j=neighbor of atom i
              Enddo
            Enddo
         Enddo
      Enddo
enddo
```

FIGURE B.4: Pseudo code for binned neighbor search.

B.6 References

1. C.L. Kelchner and S.J. Plimpton "Dislocation nucleation and defect structure during surface indentation," Phys Rev B., 58, 1998, 11085.

2. JA Zimmerman, CL Kelchner, PA Klien, JC Hamilton, and SM Foiles, "Surface step effects on nanoindentation" Phys. Rev. Letts., 87, 2001, 165507.

3. M.P Allen and D.J. Tildesley "Computer Simulations of Liquids," Oxford Science Publications. 1987, pp. 149-152